



Working Report 2015-49

Paleoclimatic Inversion of Ground Surface Temperature History from Geothermal Data on the Olkiluoto Drill Hole OL-KR56

Ilmo Kukkonen

Volker Rath

Arto Korpisalo

October 2015

POSIVA OY

Olkiluoto

FI-27160 EURAJOKI, FINLAND

Phone (02) 8372 31 (nat.), (+358-2-) 8372 31 (int.)

Fax (02) 8372 3809 (nat.), (+358-2-) 8372 3809 (int.)

Working Report 2015-49

Paleoclimatic Inversion of Ground Surface Temperature History from Geothermal Data on the Olkiluoto Drill Hole OL-KR56

Ilmo Kukkonen

University of Helsinki

Volker Rath

Dublin Institute for Advanced Studies

Arto Korpisalo

Geological Survey of Finland

October 2015

Working Reports contain information on work in progress
or pending completion.

Paleoclimatic Inversion of Ground Surface Temperature History from Geothermal Data on the Olkiluoto Drill Hole OL-KR56

ABSTRACT

We carried out paleoclimatic geothermal inversions for ground surface temperature history (GSTH) of Olkiluoto using thermal data on drillhole OL-KR56. A new temperature log extending to 1192 m (drilling depth, corresponding to 1157 m vertical depth) was obtained for the present study and rock thermal properties were measured using 262 rock specimens taken at about 5 m intervals of the drill core. At depths exceeding 100 m, heat flow density calculated in 100 m intervals varies between 32.6 and 42.7 mWm⁻². The variation of heat flow values between depth intervals is mostly higher than the technical determination errors (1.1 to 2.4 mWm⁻²).

Inversions were done using several different methods. The applied methods were (1) analytical singular value decomposition, (2) numerical method with finite differences and Tikhonov regularization, and (3) non-linear solution by finite differences and Bayesian uncertainty evaluation based on a Metropolis-Hastings Monte Carlo approach.

A pertinent feature of the results obtained with any of the inverse methods is a rather smooth behavior of the GST back to about 800 a BP, preceded by a maximum (1 – 1.5 K) higher than present) between 1000 a BP and 2500 a BP. The inversions do not yield information on conditions prior to about 2000 a BP with the exception that temperatures significantly less than modern ones are required. We attribute it is due to the limited depth of the drillhole, and the very late emergence of the drill site from the Baltic Sea at about 1000 a BP.

Keywords: Paleoclimate, ground surface temperature, inverse solutions, thermal properties of rocks, nuclear waste disposal, Olkiluoto, migmatitic rocks.

Paleoklimatologinen inversiomallinnus maanpinnan lämpötilahistoriasta Olkiluodon kairareiän OL-KR56 geotermisten mittausaineistojen perusteella

TIIVISTELMÄ

Tässä tutkimuksessa tehtiin paleoklimatologinen inversiomallinnus maanpinnan lämpötilahistoriasta Olkiluodossa käyttäen kairareiän OL-KR56 termisiä reikämittauksia ja kairasydännäytteiden laboratoriomittauksia. Reiästä tehtiin uusi lämpötilaluotaus tätä tutkimusta varten 1192 m:n kairaussyvyyteen saakka (vastaa 1157 m:n vertikaalisyvyyttä). Kiven termiset ominaisuudet mitattiin 5 m näytevälillä. Yli 100 m:n syvyydellä määritetty lämpövuoto (100 m:n syvyysjaksoissa) vaihtelee välillä 32.6 – 42.7 mWm⁻². Lämpövuotoarvojen vaihtelu syvyysvälistä toiseen on useimmiten suurempaa kuin tekniset määrittämisvirheet (1.1 – 2.4 mWm⁻²).

Inversiomallinnusta tehtiin useilla menetelmillä. Käytetyt menetelmät olivat (1) analyttinen singulaariarvohajoitelmaan perustuva inversio, (2) numeerinen äärellisen erotuksen (engl. finite difference) menetelmään ja Tikhonovin regularisointiin perustuva inversio ja (3) epälineaarinen äärellisen erotuksen menetelmään ja bayesialaiseen epätarkkuusanalyysiin perustuva Metropolis-Hastings Monte Carlo –inversio.

Kaikkien inversiotulosten yhteinen ominaisuus on, että ne indikoivat suhteellisen pientä lämpötilavaihtelua nykyhetkestä noin 800 vuotta taaksepäin. Tätä edelsi lämpötilamaksimi (noin 1- 1.5 K korkeampi lämpötila) noin 1000 – 2500 vuotta sitten (BP). Inversiomallinnus ei anna luotettavaa tietoa lämpötilahistoriasta ennen aikaa 2000 BP, lukuun ottamatta sitä, että lämpötila oli selvästi alempi. Tämä ongelma johtuu kairareiän pienestä syvyydestä sekä siitä, että Olkiluodon alue (etenkin reikäpaikka) kohosi merenpinnan yläpuolelle vasta noin 1000 vuotta sitten.

Avainsanat: Paleoilmasto, maanpinnan lämpötila, inversiomenetelmät, kivien termiset ominaisuudet, migmatiittiset kivilajit, ydinjätteen loppusijoitus, Olkiluoto.

TABLE OF CONTENTS

ABSTRACT	
TIIVISTELMÄ	
PREFACE	3
1 INTRODUCTION	5
2 MEASUREMENTS OF DRILLHOLE TEMPERATURE AND ROCK THERMAL PROPERTIES.....	7
2.1 Temperature measurements in OL-KR56	7
2.2. Measurement of thermal properties of the drillcore samples	7
3 RESULTS ON DONWHOLE AND LABORATORY MEASUREMENTS	9
3.1. Temperature, temperature gradient and heat flow density	9
4 INVERSIONS FOR GROUND SURFACE TEMPERATURE HISTORY.....	15
4.1 Analytical model with SVD	16
4.2 Nonlinear solution by FD and Tikhonov Regularization	19
4.3 Nonlinear solution by FD and Bayesian uncertainty evaluation	30
5 DISCUSSION	33
5.1 General considerations	33
5.2 Physical setup of the forward model	34
5.3 Paleoclimatic interpretation	35
6 CONCLUSIONS	41
REFERENCES	43
APPENDICES.....	49
Appendix 1: Temperature data in OL-KR56	49
Appendix 2: Results of laboratory measurements at room temperature	55

PREFACE

The study has been carried out at the University of Helsinki, Dublin Institute for Advanced Studies and Geological Survey of Finland (GTK) on contract for Posiva Oy. On behalf of the Client, the supervising of the work was done by Kimmo Kemppainen and Topias Siren (Posiva Oy). The project design, interpretation and reporting were done by Ilmo Kukkonen (University of Helsinki) and Volker Rath (Dublin Institute for Advanced Studies), and downhole measurements by Arto Korpisalo (GTK) and the laboratory measurements by Satu Vuoriainen (GTK). Jan Sundberg (GeoInnova Ab, Sweden) kindly provided data on soil and ground temperature relations at Forsmark.

1 INTRODUCTION

Paleotemperatures of the ground surface can be inverted from subsurface temperature logs in drill holes. The surface temperature of the earth is controlled by the heat transfer across the ground-atmosphere interface. It is affected by climatic conditions, type of ground surface, vegetation and thermal properties of the subsurface. Warm and cool periods at the surface affect the subsurface temperatures (Figure 1) which can be used for extracting the ground surface temperature history.

Ground surface temperatures vary in several time scales ranging from diurnal and annual cycles to as long as glacial cycles (about 100,000 years). Temperature variations on the surface propagate downward and attenuate in the subsurface medium as a diffusion signal. The daily variation extends to 0.5 – 1.0 m depth, the annual variation to 10 – 15 m, decadal and millennial variations to tens and hundreds of metres, and the ice-ages with a periodicity of the order of 100,000 years up to several kilometres, respectively. The subsurface can be utilized as a memory of past ground surface temperatures which can be extracted from drillhole temperature data with forward and inverse modelling. Due to the diffusive character of the temperature signal high-frequency information is efficiently low-pass filtered and the remaining data is useful for revealing long-term trends in ground surface temperature (GST) history. High-frequency variations can be studied with other palaeoclimatological proxies, such as tree rings and lacustrine and marine sediments. In contrast to these typical proxies applied in palaeoclimatological studies, the geothermal method does not require calibration, but provides the GST data directly from drillhole temperatures. Thermal rock properties (conductivity, diffusivity and in deep holes also heat production rate) must be known or assumed.

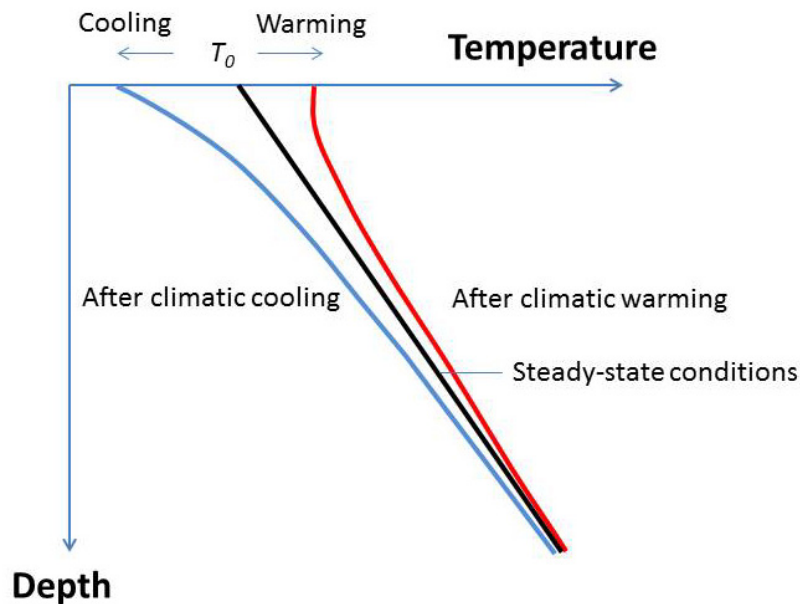


Figure 1. Schematic presentation of subsurface temperature response on climatic cooling or warming of the average ground surface temperature.

Drillhole depth constrains the time range of the GST history that can be extracted from temperature logs. Holes extending to 500 – 1000 m are useful for the last one-two millennia, but holes extending to about 1.5 – 2 km can be used for estimating the GST history during the last 50 – 100 ka.

Inversion of GST history from drillhole temperature logs has been extensively applied for paleoclimatic studies since the 1980's. Although the effect of paleotemperatures on measured drillhole temperatures has been known for long (e.g. Benfield 1949, Birch 1948), and heat flow data has been routinely corrected for climatic effects (e.g. Jessop, 1971, Beck, 1977, Kukkonen 1987), the utilization of subsurface temperature data as a source for paleotemperature information emerged when inversion methods were taken into use in the problem. Several methods have been applied for the GST inversion, but the most common ones are the singular value decomposition (SVD) method (Beltrami and Mareschal, 1992, Beltrami et al., 1997), functional space inversion (Shen and Beck, 1991), Monte Carlo inversion (Mareschal et al. 1999, Kukkonen and Jöeleht 2003, Haario et al., 2006), and numerical methods using Tikhonov regularization (Rath and Mottaghy, 2007) and Bayesian uncertainty estimation (e.g. Mosegaard & Tarantola 1995, 2002; Tarantola, 2005). In these methods the model geometry is constrained to a homogeneous half-space or a 1D layered earth. More complicated geometries must be modelled with forward methods (e.g., Kukkonen and Šafanda, 1996). However, the lack of detailed spatial information on temperatures and thermal properties in the bedrock in typical research data sets makes the use of full 2D and 3D geometries unnecessary in most cases. The state of the art in the interpretation of drillhole temperatures is presented in the recent reviews by González-Rouco et al. (2009) and Bodri & Cermak (2007).

In the present study we have applied the geothermal GST inversion methods on temperature and thermal property data from the Olkiluoto deep drillhole OL-KR56 (1158 m vertical depth) for extracting the GST history on the drilling site. The drillhole is the deepest at the moment in Olkiluoto. The existing previous temperature logs from Posiva archives were first analysed for the purpose of the present study and due to significant differences between them a new log was obtained in April 2014. To be able to take into account the effects of thermal property variations with depth, we measured thermal conductivity, specific heat capacity and density at 5 m intervals in the laboratory, using altogether 262 drill core samples.

We provide comparison of results obtained with several inversion methods, and discuss the Olkiluoto GST history in terms of the Weichselian glaciation, and the Holocene climatic changes. The Olkiluoto GST data is especially challenging to interpret due to the different marine stages of the Baltic Sea between the deglaciation (about 11 ka BP) and until about 1000 years BP when the drilling site finally emerged from the sea.

2 MEASUREMENTS OF DRILLHOLE TEMPERATURE AND ROCK THERMAL PROPERTIES

2.1 Temperature measurements in OL-KR56

The field work in Olkiluoto was carried out on April 24, 2014. The drilled depth of the hole is 1248 m, but we could reach only 1191.6 m depth, most probably due to problematic fracture zones present at that depth.

Logging was done using the point-by-point technique with a memory logger probe (type Antares, ser.no. 1854358, manufacturer Antares GmbH, Germany). The instrument has a resolution of 1.2 mK at 20°C and 0.75 mK at 1°C. The absolute accuracy is ± 0.1 mK and the time constant of the instrument is 2 s. The applied station interval was 2.5 m and the probe was kept stationary at each station for 1 min. Temperature readings were saved at 1 s intervals. The Antares temperature probe was attached to the lower end of the TERO logging cable (Kukkonen et al. 2014) and lowered to the drillhole. Data was collected in the downward logging direction. Data was downloaded after logging from the memory chip of the probe.

The logging depth and time were measured with the measuring wheel of the TERO in situ thermal conductivity device (Kukkonen et al. 2014) and saved in a separate file on a PC. In the office the two files (temperature vs. time and depth vs. time) were correlated into a single depth-temperature file. Temperature values were picked from the equilibrated part of the record at each depth where the temperature variation had stabilized below 1 mK.

Vertical depth values were calculated using the dip data measured at 5 m intervals and provided by Posiva. The hole is sub-vertical with the dip decreasing from 84° at the surface to 73° at the bottom of the hole. The maximum drilling depth reached (1191.6 m) corresponds to a vertical depth of 1157.2 m.

Numerical temperature data are listed in Appendix 1.

2.2. Measurement of thermal properties of the drillcore samples

The laboratory measurements were done at the petrophysical laboratory of the Geological Survey of Finland in 2013–2014. The OL-KR56 drillcore was sampled at 5 m intervals (specimens provided by Posiva) and ca. 7 mm thick disks were cut, surfaces were prepared parallel and polished (polishing powder no. 180 for finishing). Thermal conductivity samples represent conductivity along the drillcore axis.

Rock thermal properties were measured using the divided-bar method for thermal conductivity, calorimetric method for specific heat capacity and air-water weighing for bulk density. Diffusivity was calculated from measured values of conductivity, specific heat and density. The measurement and reduction methods are the same as used in previous measurements of Olkiluoto rock thermal properties and described in detail in Kukkonen et al. (2011a). Conductivity was measured after saturating the samples for 2 days in tap water at ambient pressure and temperature. Foliation angle of the samples was measured from the conductivity samples.

Numerical laboratory data are listed in Appendix 2.

3 RESULTS ON DONWHOLE AND LABORATORY MEASUREMENTS

3.1. Temperature, temperature gradient and heat flow density

The temperature log of OL-KR56 is shown in Figure 2 along with a reduced temperature log. The reduction was done by subtracting a constant gradient of 13.5 mK m^{-1} from the measured values. As a result of the reduction, the local temperature variations can be easily seen. To a depth of about 45 m the temperature log reflects the annual cycle and very recent temperature variations during the last ~ 10 years and may be related to climatic warming and changes in the ground surface due to drill site construction. The deeper part seems to be characterized by a relatively steady gradient of about 13.5 mK m^{-1} between 45 and 750 m, and beneath that a higher gradient of about 15.5 mK m^{-1} to the hole bottom. The reduced temperature log reveals small local variations especially at depths exceeding 750 m. In the original log these variations are of the order of a few hundredths of K only, and we attribute these to minor flow effects between the hole and permeable fractures. Reduced temperature log is compared with conductivity and density data in Figures 3 and 4, respectively.

Conductivity values are usually between 2.0 and $3.5 \text{ W m}^{-1} \text{ K}^{-1}$ and the hole average is $2.57 \pm 0.49 \text{ W m}^{-1} \text{ K}^{-1}$. Values outside this range are due to exceptional mineral composition (e.g., content of graphite) or high angles of foliation together with low quartz content. Density average is $2713 \pm 69 \text{ kg m}^{-3}$.

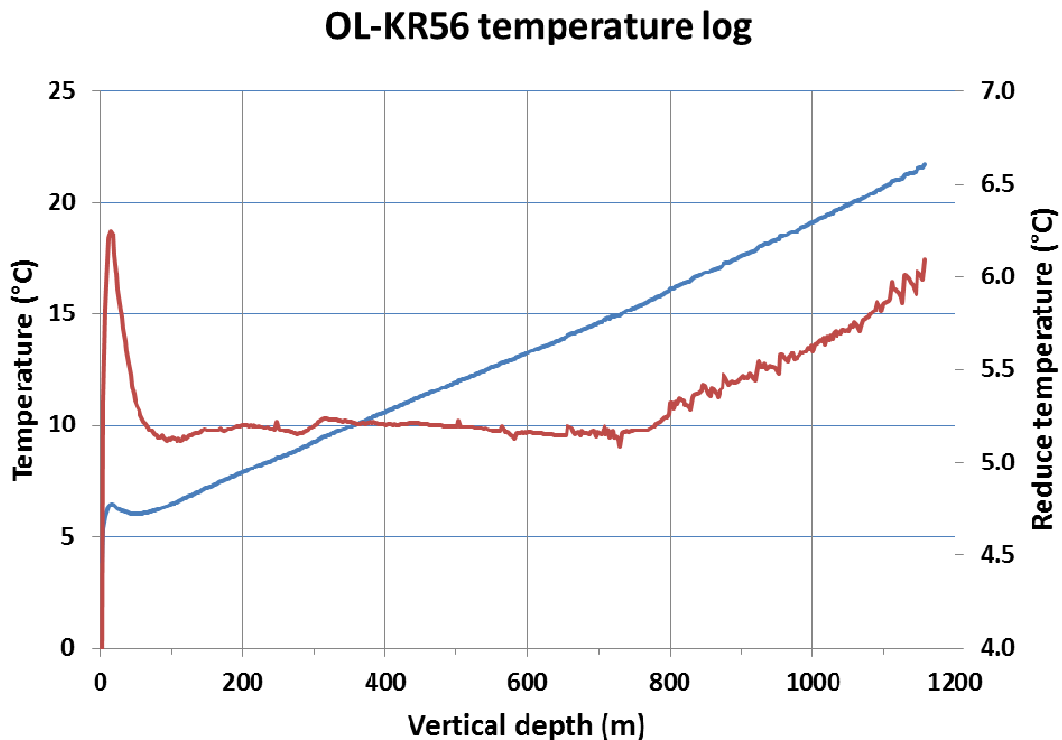


Figure 2. Temperature log (blue) of drillhole OL-KR56 measured in April 2014. The reduced temperature log (red) was calculated by reducing a constant gradient of 13.5 mK m^{-1} from the measured values.

OL-KR56 reduced T and conductivity

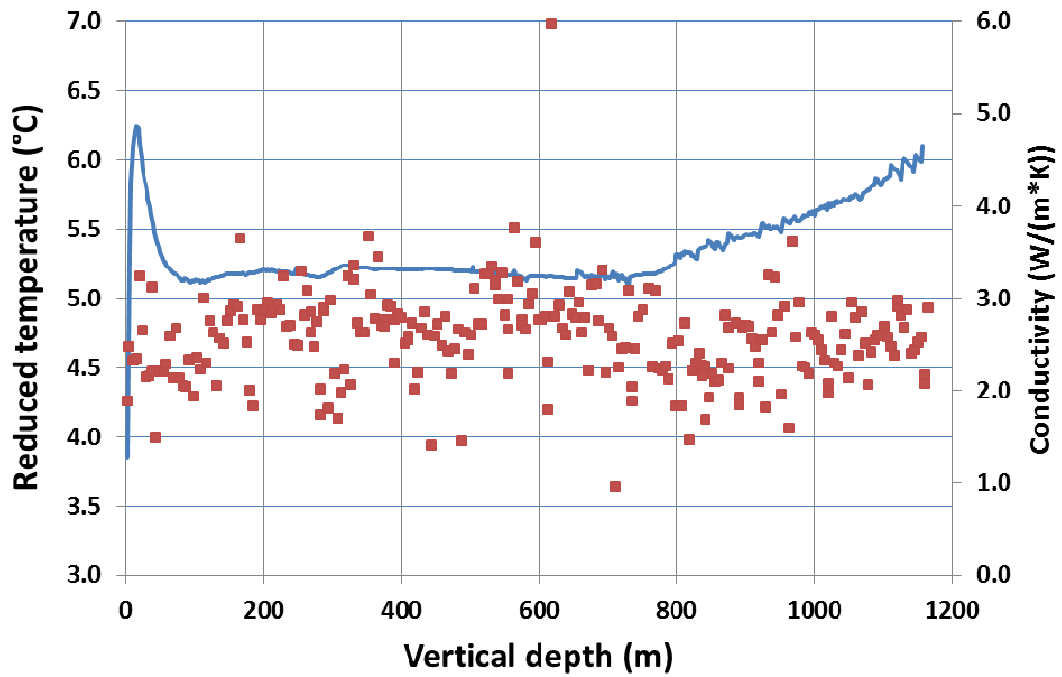


Figure 3. Reduced temperature (blue line) and measured thermal conductivity in OL-KR56.

OL-KR56 reduced T and density

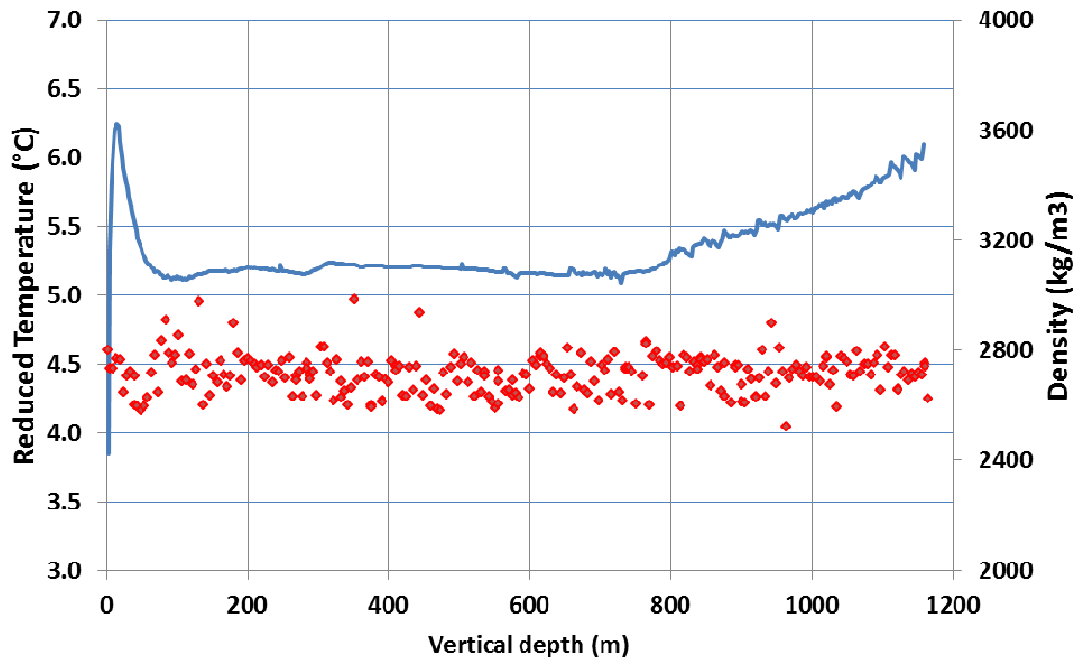


Figure 4. Reduced temperature (blue line) and measured rock bulk density in OL-KR56.

Conductivity shows a weak decreasing trend with increasing foliation angle (Figure 5) in a similar way that has been observed in Olkiluoto rocks in previous studies (Kukkonen et al. 2011a). The correlation coefficient is, however, small ($R = 0.21$).

Conductivity vs. density plot repeats the trends found already previously in Olkiluoto rocks. For gneissic rocks (VGN, TGG, DGN), there is a general decreasing trend of conductivity with increasing density. In terms of mineral composition it can be attributed to the content of quartz which has a conductivity value ($\sim 7.7 \text{ Wm}^{-1}\text{K}^{-1}$) well above the rock type averages but a density (2630 kgm^{-3}) below the average values. This trend does not seem to apply to MGN which shows more scattered values in the plot. For pegmatitic granite (PGR) the trend is opposite, and conductivity increases steeply with increasing density. Once again, the variations represent only data trends and not distinct correlations. The results are in agreement with the earlier findings reported in Kukkonen et al. (2011a).

Temperature gradient, thermal conductivity and heat flow density values are shown in Table 1. At depths exceeding 100 m, heat flow density calculated in 100 m intervals varies between 32.6 and 42.7 mWm^{-2} . The variation between depth intervals is mostly higher than the technical determination errors ($1.1 - 2.4 \text{ mWm}^{-2}$).

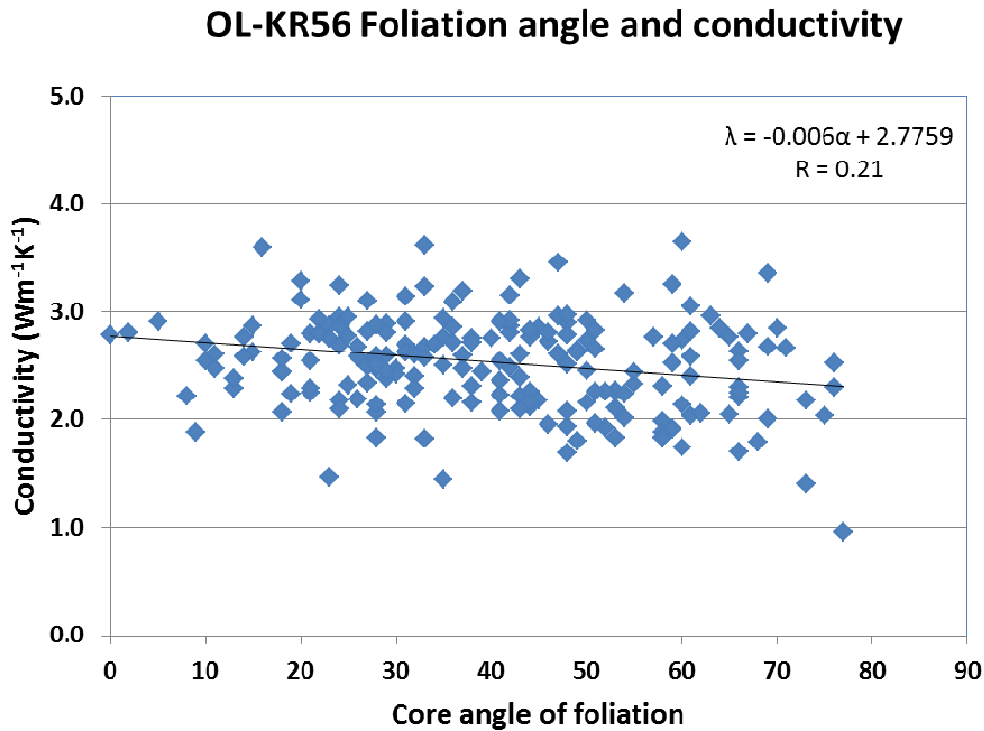


Figure 5. Thermal conductivity vs. core angle of foliation in OL-KR56 core samples (only gneissic rock types included). Foliation angle 0° corresponds to the conductivity direction parallel to gneissic foliation, and 90° perpendicular to it.

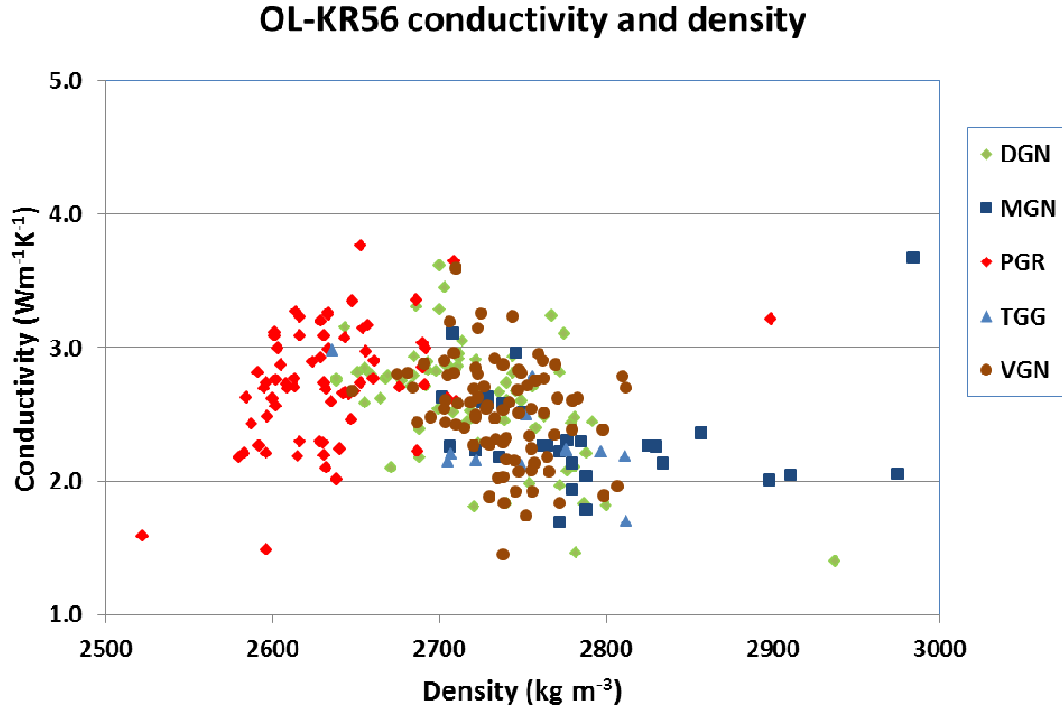


Figure 6. Thermal conductivity vs. density in OL-KR56.

Table 1. Conductivity, temperature gradient and heat flow data on OL-KR56.

Depth	Conductivity	Std	Mean error	N (cond)	Gradient	Error	Heat flow	Error
(m)	(Wm ⁻¹ K ⁻¹)	(Wm ⁻¹ K ⁻¹)	(Wm ⁻¹ K ⁻¹)		(mKm ⁻¹)	(mKm ⁻¹)	(mWm ⁻²)	(mWm ⁻²)
22-50	2.35	0.48	0.14	12	-11.6	0.6	-27.3	-0.2
50-100	2.24	0.24	0.08	10	9.9	0.3	22.2	1.5
100-200	2.61	0.41	0.09	20	14.3	0.1	37.4	1.5
200-300	2.71	0.39	0.08	24	13.1	0.1	35.5	1.2
300-400	2.73	0.49	0.10	23	13.3	0.0	36.3	1.5
400-500	2.44	0.39	0.08	22	13.4	0.0	32.6	1.2
500-600	2.99	0.35	0.07	23	13.0	0.1	38.8	1.1
600-700	2.87	0.78	0.17	22	13.5	0.1	38.9	2.4
700-800	2.38	0.49	0.10	22	14.4	0.1	34.3	1.8
800-900	2.23	0.36	0.07	23	15.0	0.1	33.5	1.4
900-1000	2.55	0.47	0.10	22	15.1	0.1	38.6	1.8
1000-1100	2.46	0.26	0.06	22	15.7	0.1	38.6	1.1
1100-1158	2.64	0.20	0.06	13	16.2	0.5	42.7	2.3
100-750	2.70	0.52	0.04	100	13.5	0.01	36.4	0.6
750-1158	2.45	0.38	0.04	140	15.5	0.02	37.8	0.6

The variation may be partly due to the relatively short depth intervals applied and large local variations in thermal conductivity along with (still) small number of conductivity measurements in each interval. Further, 2D and 3D conduction effects may also contribute in the result.

The reduced temperature and calculated gradient reveal an increase in gradient at about 750 m (Figures 7 and 8), but the average heat flow values above (at 100 – 750 m, $36.4 \pm 0.6 \text{ mWm}^{-2}$) and below (750 – 1158 m, $37.8 \pm 0.6 \text{ mWm}^{-2}$) are not essentially different, because the gradient change is compensated with thermal conductivities being slightly higher (2.70 ± 0.52 (1 std) $\text{Wm}^{-1}\text{K}^{-1}$) at 100 – 750 m than beneath ($2.45 \pm 0.38 \text{ Wm}^{-1}\text{K}^{-1}$) (see Table 1).

The heat flow and gradient contrast at 750 m is quite small and could be attributed to paleoclimatic factors (as we assume below). In principle it could also be attributed to hydrogeological effects. Steady (long-term) fluid flow in an inclined fracture zone could produce such a heat flow change (Drury 1984, Lewis and Beck 1977). The hydrogeological data on OL-KR56 (Toropainen, 2012; Ripatti et al., 2013) shows a brittle fault zone at 751 – 772 m vertical depth, but there are no significant hydraulically permeable fractures at this depth interval. The drillhole intersects 12 brittle fault zones altogether, and most of them are permeable. However, they do not seem to affect the heat flow data significantly (Figure 7).

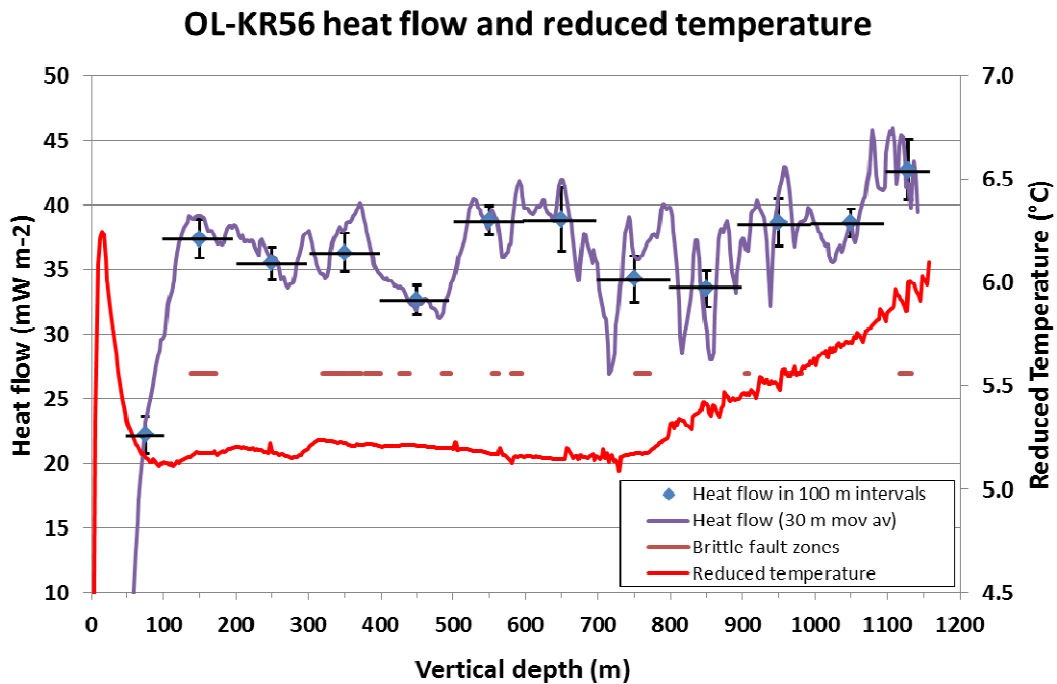


Figure 7. Heat flow density values calculated in 50 – 100 m depth intervals (blue diamonds with error bars) (Table 1), heat flow calculated with 30 m moving averages of conductivity and gradient (lilac line) together with reduced temperature log (red line). The brown horizontal bars represent the depths of brittle fault zones.

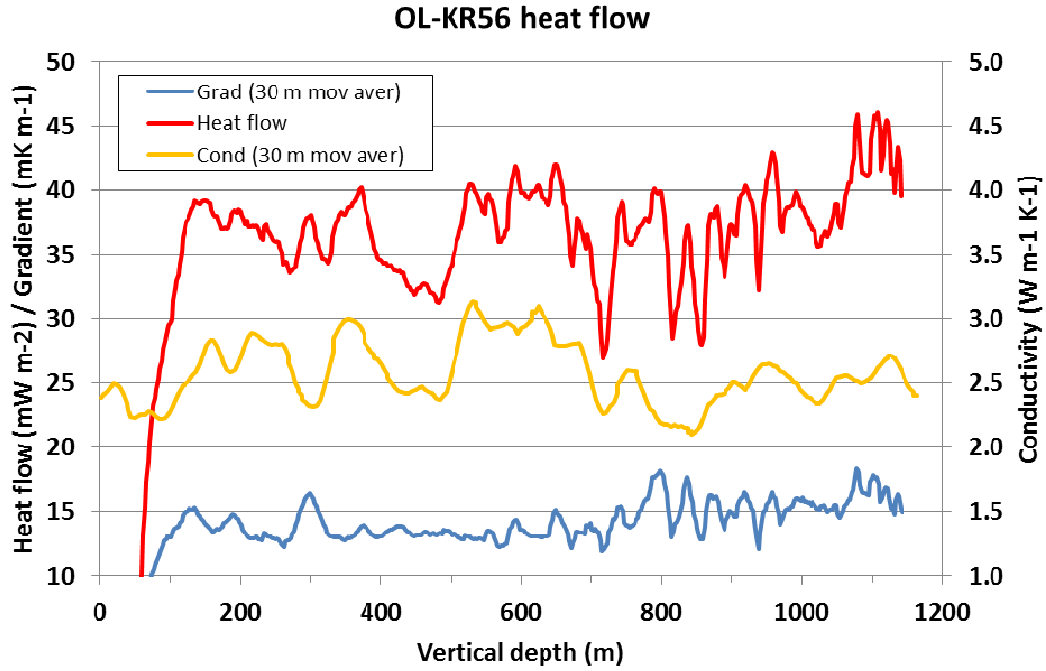


Figure 8. Heat flow density (red line) calculated with 30 m moving averages of gradient (blue) and thermal conductivity (yellow).

Comparison of conductivity and gradient variations (Figure 8) allows some insight to the heat transfer mechanisms present in the rock. If the rock can be considered a 1D layered earth, the heat flow vector is vertical and thermal conductivity and gradient are locally inversely correlated. However, the correlation fails when the conductivity varies in 2D and 3D and the heat flow vector is not anymore vertical. The effect increases with increasing conductivity variation and is also dependent on the drillhole dip (Kukkonen et al. 2011b). In OL-KR56 conductivity minima are often correlated with gradient maxima and vice versa, but there are also sections where such a behavior is absent, e.g. at 400 – 600 m, where the gradient is practically constant but conductivity shows strong variations (Figure 8). Such effects may be indeed be due to 2D and 3D conduction effects (refraction of heat), but may also reflect the heterogeneity of conductivity in the small scale, and sampling the rock with a practically point-like (7 mm × 42 mm) samples at 5 m intervals. The conductivity variations observed in the data might be different with a different sample size and sampling interval. As the gradient varies relatively little, the local heat flow variations are mostly due to variations in conductivity.

4 INVERSIONS FOR GROUND SURFACE TEMPERATURE HISTORY

The task of deriving meaningful estimates of past climate changes, in particular ground surface temperature histories (GSTH), from recent borehole temperature profiles (BTP) is nontrivial, because the problem is strongly ill-posed in the sense of Hadamard 1923). This means that in a mathematical sense, the solutions to this problem may not exist, they are non-unique, and possibly inherently instable. Hansen (1998, 2010) and Aster et al. (2013) give detailed accounts of this concept, and the techniques necessary to solve this kind of problems. In practice, this implies that the observed data (in this case the temperature measurements) need to be combined with knowledge from other sources to render the problem tractable. For the Olkiluoto drillhole, this additional (prior) information includes a set of measured petrophysical properties, some assumptions on the (forward) model used for the simulations, and on the general character of the solutions. It follows directly, that in these studies, the goodness-of-fit cannot be the single criterion for the quality of the solution.

Most current software for the estimation of GSTHs from drillhole temperature profiles is based on a one-dimensional, conduction-only forward model. Thermal conduction in rocks is based on the partial differential equation (PDE)

$$(\rho c)_e \frac{\partial T}{\partial t} + \frac{\partial}{\partial z} \left[\lambda_e \frac{\partial T}{\partial z} \right] - H = 0 \quad , \quad (1)$$

which is solved with the appropriate boundary conditions of

$$T_0(z_0, t) = T_{GS}(t)$$

at the surface and

$$\frac{\partial T}{\partial z} = -\frac{Q_b}{\lambda_e}$$

at the base of the model domain. In (1), the index e denotes effective properties, i.e., properties which describe the rock-fluid two-phase system. Since porosity is very low in this study (<1%, see Posiva Oy, 2013), all properties will represent rock properties, and the e index will be omitted. The occurring physical parameters are the density ρ (kg m⁻³) heat capacity c_p (J kg⁻¹K⁻¹), and thermal conductivity λ (Wm⁻¹K⁻¹) (Figure 9). H (Wm⁻³) denotes the volumetric radiogenic heat production, which is neglected here.

In the following we will first describe the physical setup for the inverse modeling, then present results from three different inversion methods: (1) a linear method using singular value decomposition (SVD, see Lanczos 1961, Hansen 1998) of the system matrix; (2) a nonlinear method based on generalized Tikhonov regularization combined with a finite difference solver for the corresponding partial differential equation (1) (Rath & Mottaghy 2007) and (3) a Bayesian procedure using Markov Chain Monte Carlo (MCMC) sampling (e.g. Mosegaard & Tarantola 1995, 2002; Tarantola, 2005) with the same forward model.

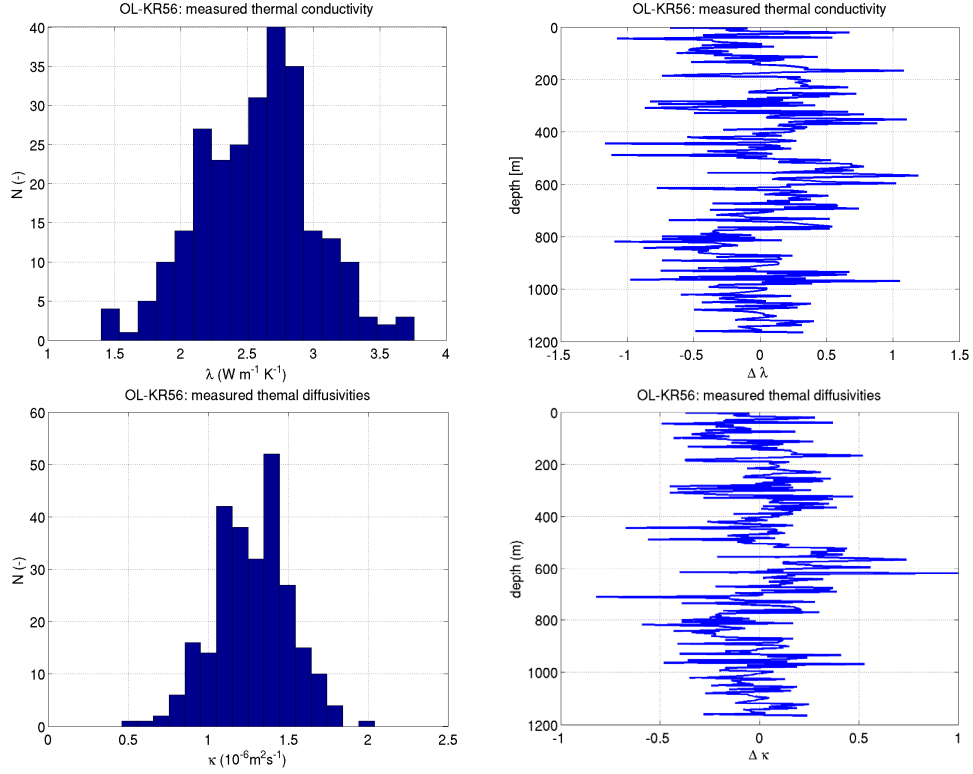


Figure 9. Rock properties used in the inverse modelling of OL-KR56. Top left: Thermal conductivity, histogram; Top right: Perturbation with respect to the average value; Bottom left: Diffusivity, histogram; Top right: Perturbation with respect to the average value.

4.1 Analytical model with SVD

A common simplification is to assume thermal conductivity λ which does not depend on depth, which leads to the simpler PDE

$$\frac{\partial T}{\partial t} = \kappa \frac{\partial^2 T}{\partial z^2} + \frac{H}{\rho c}, \quad (2)$$

where the thermal diffusivity,

$$\kappa \equiv \frac{\lambda}{\rho c},$$

was introduced. In this case an analytical solution can be found for a GST composed of K step functions T_k at times t_k (Carslaw & Jaeger, 1959). This solution,

$$T(z, t) = T_{stat}(z) + T_{trans}(z, t),$$

consists of two parts. T_{stat} represents the stationary geothermal profile determined by a virtual surface temperature T_0 , thermal conductivity λ , and the basal heat flow density Q_b :

$$T_{stat}(z) = T_0 + \frac{Q_b}{\lambda} z, \quad (3)$$

where radiogenic heat production has been neglected. The transient part can be written as

$$T_t(z, t) = \sum_{k=1}^K T_k \left[\operatorname{erfc} \left(\frac{z}{2\sqrt{\kappa t_k}} \right) - \operatorname{erfc} \left(\frac{z}{2\sqrt{\kappa t_{k-1}}} \right) \right]. \quad (4)$$

A discrete version of the transient part of the solution leads to the linear matrix equation

$$\mathbf{T}^{obs} = \mathbf{M} \mathbf{T}^{gst}, \quad (5)$$

where \mathbf{T}^{obs} is a vector of measured drillhole temperatures at N depths z_n . \mathbf{T}^{gst} is the vector of K discrete steps T_k at times t_k . A detailed derivation of this equation was lately given by Brynjarsdottir and Berliner (2011).

Equation (5) needs to be inverted to estimate the \mathbf{T}^{gst} . Beltrami & Mareschal (1992) introduced an approach based on a damped singular value decomposition (DSVD) to the context of GST estimation that has since been a standard tool for analyzing drillhole temperatures as paleoclimatic indicators. In this method, stabilization is achieved by replacing the singular values σ_i on the diagonal of \mathbf{S} in the SVD,

$$\mathbf{M} = \mathbf{U} \mathbf{S} \mathbf{V}^T,$$

by

$$\tilde{\sigma}_i = \frac{\sigma_i}{\sigma_i^2 + \varepsilon^2},$$

using an appropriate regularization parameter ε . As pointed out by Aster et al. (2013), this is equivalent to a standard Tikhonov regularization with regularization parameter ε^2 . A generalized inverse can then be formed, and the regularized solution can be found by

$$\mathbf{T}^{gst} = \mathbf{M}_{\varepsilon}^g \mathbf{T}^{obs} = \mathbf{V} \mathbf{S}_{\varepsilon}^{-1} \mathbf{U}^T \mathbf{T}^{obs}. \quad (6)$$

Many methods exist to determine the optimal value of ε (Hansen, 1998, 2010). In this study we applied the L-curve method or the generalized cross-validation (GCV) methods (Hansen 1998, 2010; Aster et al. 2013; Vogel 2002).

In addition to the temperature steps of the GSTH, this method requires the determination of the equilibrium surface temperature T_0 , and the measured geothermal heat flow density Q_b data. Assuming uniform thermophysical properties of the subsurface a simple estimate of the geothermal gradient can be calculated from the linear trend at the deepest part of the temperature profile, which is assumed to be least affected by the recent ground temperature changes. In that case, T_0 then follows from upward continuation of this linear trend. However, in this study we have included both parameters into the set of parameters to be inverted.

Experimental setup

The inversion of drillhole temperatures using the forward model described above requires not only the setup of the model itself, but some pre-processing of the inputs, data as well as rock properties. Depending on the degree of complexity of the assumed geological structure and target ground surface temperature history different options exist.

For the highly simplified analytical solution presented below, the only consistent possibility is the use of appropriate average values for the physical variables. From the thermal properties of OL-KR56 measured on the core material, we estimated the average values given in Table 2 below.

Table 2. Average values for the rock properties used in the inversions. In addition to the means and standard deviations in the first line, we also give the medians and mean absolute deviations in the second.

	λ (Wm ⁻¹ K ⁻¹)	ρ (kg m ⁻³)	c_p (J kg ⁻¹ K ⁻¹)	κ (10 ⁻⁶ m ² s ⁻¹)
$m_{avg} \pm m_{std}$	2.6±0.4	2710±60	743±16	1.275±0.23
$m_{med} \pm m_{mad}$	2.6±0.3	2720±50	741±13	1.290±0.18

Results

The inversions presented here were run with a parameter vector consisting of 32 logarithmically evenly spaced temperature steps, with the equilibrium surface temperature T_0 , and the basal heat flow density Q_b added. However, the numerical experiments led to the conclusion that this method may not be adequate in this case.

The optimal ε derived from the L-curve (as well as from the other criteria mentioned above) is ≈ 0.04 , while a much larger value (> 0.2) is needed to produce a credible result. The L-Curve does not show the ideal form, as it shows a constant gradient between $\varepsilon = 0.6$ and 0.05. This is mainly due to the assumption of constant thermal properties, which represents a model error, which is falsely treated as signal in the inversion procedure. In Figure 10 it is clearly visible, that the better fit of the optimally regularized solution is the result of an improved fit to the derivations from the average properties. The estimated background heat flow density and equilibrium ground temperatures for both cases are ≈ 38 mWm⁻² and 4.8°C, respectively. This agrees well with the results of Rath et al. (2012).

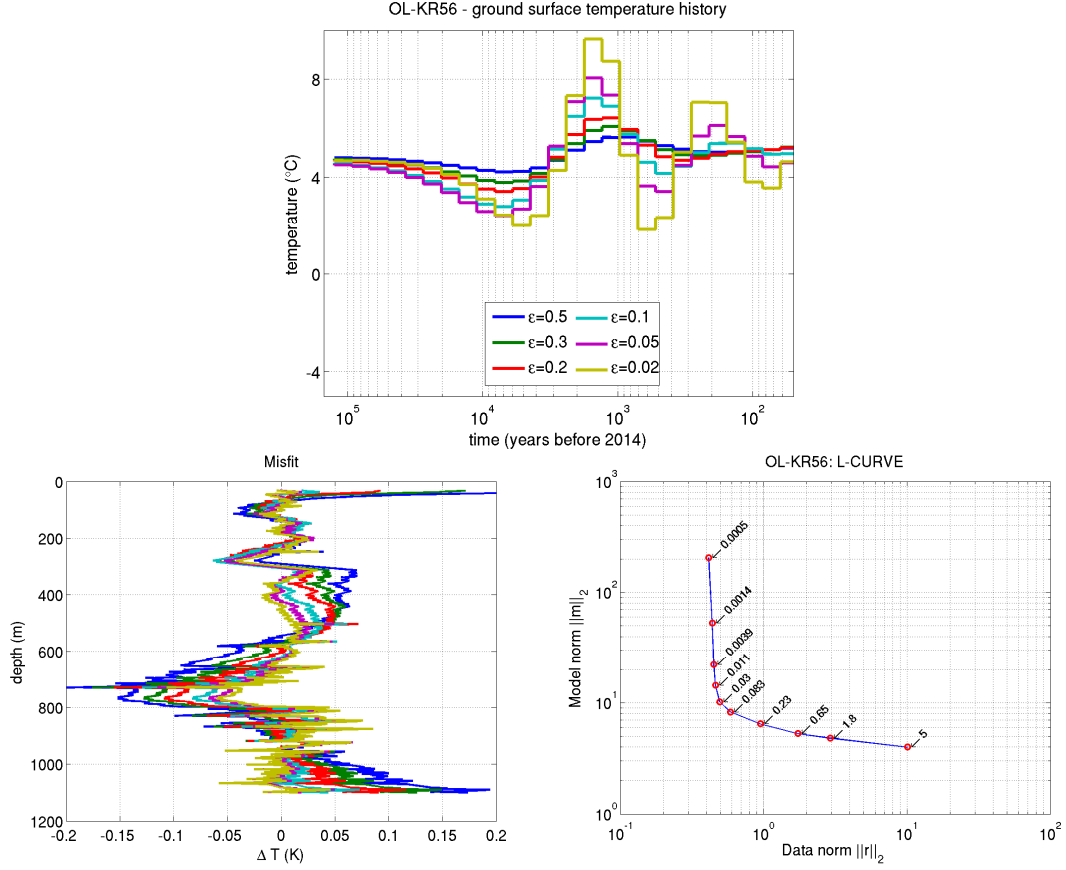


Figure 10. Top: Results from SVD inversions. The optimal ϵ derived from the L-curve (as well as from the other criteria mentioned in the text) is ≈ 0.04 , but a much larger value ($\epsilon > 0.2$) is needed to produce a credible result (green and blue curves). This is probably because the algorithm improves fit by approximating the residuals originating from the model error. Left: residuals $\mathbf{r} = \mathbf{T}_{obs} - \mathbf{T}_{calc}$. Right: L-Curve. The estimated HFD and surface temperature are 38 mWm^{-2} and 4.8°C , respectively.

4.2 Nonlinear solution by FD and Tikhonov Regularization

In contrast to the method described above, the forward problem is solved by numerical finite difference techniques, allowing for a flexible discretization both in time and space. For the particular problem of drillhole paleoclimate models, which extend back to more than 100 ka BP, a logarithmic time stepping is chosen, starting with very large steps, which are reduced to very short ones near the present. This matches the physical character of the underlying conductive process, which reduces the high-frequency content of the GSTH with increasing depth. Details are given in (Mottaghy & Rath 2006) and (Rath & Mottaghy 2007). The vertical discretization relevant to the upscaling process is sketched in Figure 11.

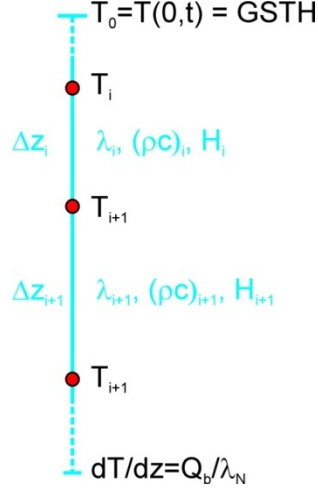


Figure 11. Schematic description of the discretization used for the FD forward modelling. Measured data have to be assigned to computational nodes (red), while the properties are associated with the cells. Both may imply interpolations or averaging (upsampling) to a given grid for observed temperatures and measured petrophysical properties.

For the inversions presented here we used the variational approach presented in (Rath & Mottaghy 2007) to determine a stable model, and a Metropolis-Hastings Markov Chain Monte Carlo algorithm (MCMC) (Metropolis et al., 1953; Hastings, 1970) for characterizing the uncertainty, which will be presented in the following Section 4.3.

For the deterministic approach we try to minimize an objective function θ with respect to a given model specified by a set of parameters $\mathbf{m} = [m_1, m_2, \dots, m_M]$, which is defined by

$$\theta = (\mathbf{d} - \mathbf{g}(\mathbf{m}))^T \mathbf{W}_d^T \mathbf{W}_d (\mathbf{d} - \mathbf{g}(\mathbf{m})) + R(\mathbf{m} - \mathbf{m}_a), \quad (7)$$

where \mathbf{W}_d denotes a weighting matrix commonly used to standardize the residuals $\mathbf{r} = \mathbf{d} - \mathbf{g}(\mathbf{m})$, i.e. it is set to the inverse square root of the data covariance matrix \mathbf{C}_d . In Equation (7), the first term measures the data fit, while the second, $R(\mathbf{m})$, is necessary to stabilize the generally ill-posed inverse problem (see Aster et al., 2013).

In the problem treated here, the parameter vector \mathbf{m} is composed of a piecewise constant function with of time, using a logarithmic spacing. The data vector $\mathbf{d} = H(\mathbf{d}_{obs})$ contains the result of an observation operator H applied to the discrete values of temperature measured in the drillhole. In this case, the application of this operator refers to the “upsampling” procedures mentioned later.

This regularization in Equation (7) can be achieved in many different ways. Most of the results presented here use a generalized Tikhonov regularizer, formulating the corresponding term as

$$R(\mathbf{m} - \mathbf{m}_a) = \tau_0 (\mathbf{m} - \mathbf{m}_a)^T (\mathbf{m} - \mathbf{m}_a) + \sum_k \tau_k (\mathbf{m} - \mathbf{m}_a)^T \mathbf{W}_k^T \mathbf{W}_k (\mathbf{m} - \mathbf{m}_a). \quad (8)$$

In this equation, we define \mathbf{W}_k to be a discrete approximation to the first or second derivative of the parameters with respect to logarithmic time (see Aster et al. 2013), which can be written in discrete form using a logarithmic time step Δ :

$$\mathbf{W}_1 = \frac{1}{\Delta} \begin{bmatrix} -1 & 1 & \cdots & 0 \\ & -1 & 1 & \\ \vdots & & \ddots & \vdots \\ & & & -1 & 1 \\ 0 & \cdots & & -1 & 1 \end{bmatrix} \quad \mathbf{W}_2 = \frac{1}{\Delta^2} \begin{bmatrix} -2 & 1 & \cdots & 0 \\ 1 & -2 & 1 & \\ \vdots & & \ddots & \vdots \\ & & & 1 & -2 & 1 \\ 0 & \cdots & & 1 & -2 & 1 \end{bmatrix} \quad (9)$$

Taking the derivative of (7) and imposing the minimum conditions leads to the iterative system

$$\left(\mathbf{J}_w^T \mathbf{J}_w + \sum_{i=0}^1 \tau_i \mathbf{W}_{m,i}^T \mathbf{W}_{m,i} \right) \delta \mathbf{m}_k = \mathbf{J}_w^T [\mathbf{d} - \mathbf{g}(\mathbf{m}_k)] - \sum_{i=0}^1 \tau_i \mathbf{W}_{m,i}^T \mathbf{W}_{m,i} (\mathbf{m}_k - \mathbf{m}_a) \\ \mathbf{m}_{k+1} = \mathbf{m}_k + \mu \delta \mathbf{m}_k. \quad (10)$$

The weighted Jacobian and the Generalized Inverse are defined as

$$\mathbf{J}_w \equiv \mathbf{W}_d \mathbf{J} = \mathbf{W}_d \partial \mathbf{g} / \partial \mathbf{m}, \quad \mathbf{J}_w^\dagger = \left(\mathbf{J}_w^T \mathbf{J}_w + \sum_{i=0}^1 \tau_i \mathbf{W}_{m,i}^T \mathbf{W}_{m,i} \right)^{-1} \mathbf{J}_w^T, \quad (11)$$

respectively. Note that the inverse in Equation (11) is a posterior covariance matrix. These quantities are appropriate tools to further analyze the sensitivity of given data to the inverse parameters.

Given the two regularization parameters τ_0 and τ_1 , this formulation can be regarded as an approximation to an inverse spatial exponential covariance matrix in a logarithmic scale with given error and correlation length (Tarantola, 2005). For the inversions shown below, τ_0 is set to a fixed small value (0.003), while τ_1 is set to an optimal value determined by Generalized Cross Validation (Rath & Mottaghy, 2007; Farquharson & Oldenburg, 2004; Wahba, 1990). This optimal value is found by minimizing the GCV function over a set of predefined values of the regularization parameter τ .

$$GCV(\tau) = \frac{N \|\mathbf{d} - \mathbf{g}(\mathbf{m}_\tau^k)\|_2^2}{\text{trace}(\mathbf{I} - \mathbf{J}_w \mathbf{J}_w^\dagger)^2} = \min! \quad (12)$$

For the inversions presented here, we always used the GCV criterion. The UPRE criterion described in Vogel (2002) produced nearly identical results. We did not use the L-curve approach described above, as this technique is not well adapted to non-linear inverse problems, where the identification of the point of maximal curvature often leads to highly improbable results.

Experimental setup

For the finite difference (FD) model employed, the temperature data as well as the rock properties measured in the laboratory are not known at the nodes or cell centers of the numerical FD model. Thus, it is necessary to upscale or interpolate these point measurements to the nodes or cell centers, respectively. In addition, for numerical reasons the model has to extend to large depths in order to avoid undesirable effects of the boundary conditions. Thus, thermophysical properties have to be assigned for domains which are not sampled by measurements.

For drillhole OL-KR56 temperatures were available with an approximate sampling interval of about 2.5 m. As the upper 80 m is strongly influenced surface activity and is not considered reliable for paleoclimatic interpretation, we started the set of observational data at this depth. Also the observations with a depth >1120 m were excluded due to strong gradient variations, probably due to local fluid flow effects. For the densely measured temperatures, we chose either a mesh identical with the measuring depths in the corresponding interval, or using smoothing splines, or an appropriate moving average (triangular or boxcar weights, width approx. 10 m) for the approximation at the nodes. This also allowed us to estimate the interpolation error associated with these values. It is generally smaller than the uncertainty related to the non-resolved heterogeneities of rock properties, which was generally set to 0.1 K. The overall data fit is only weakly sensitive to the approximation at the nodes.

Rock properties have been measured for the whole depth of the drillhole. However, these properties (thermal conductivity λ , density ρ , specific heat capacity c_p and diffusivity κ) are sampled less densely than the temperatures, and hence pose some difficulties. From visual inspection, and in accordance with the published lithology (Posiva Oy, 2013), no obvious layering can be derived, except a slight dependence of λ on depth, which is also visible in Figures 7 and 8. Cluster analysis, which was used to discriminate different rock types (see Figure 12), produced no significant clusters in λ - ρ - c - z space, which could be used for discriminating geological layers (Figure 12). This is consistent with the findings of Kukkonen & Peltoniemi (1998) on Finnish rocks.

For this reason we decided to test several upscaling methods, including overall averages. After many experiments, we arrived at the following work flow for determining the cell properties. We collect the values which are available in the domain of a given cell. Then an appropriate weighted average is used to determine the mean, i.e., the harmonic or geometric mean for the thermal conductivity, and the arithmetic for the others (Hartmann et al., 2005; Hartmann, 2008). The former choice is due to the disputable assumption that the heat flux is dominantly vertical. The averaging procedure, however, has only a minor influence on the inversion results. The empty cells are then filled with global average values. The sampled parameters were smoothed either with a robust spline with low degrees of freedom, or a moving average with 40 – 80 m window length. An example is given in Figure 13 (bottom row). Direct use of the sampled values would lead to unphysically high variability near boundaries. Results of upscaling are shown in Figure 14.

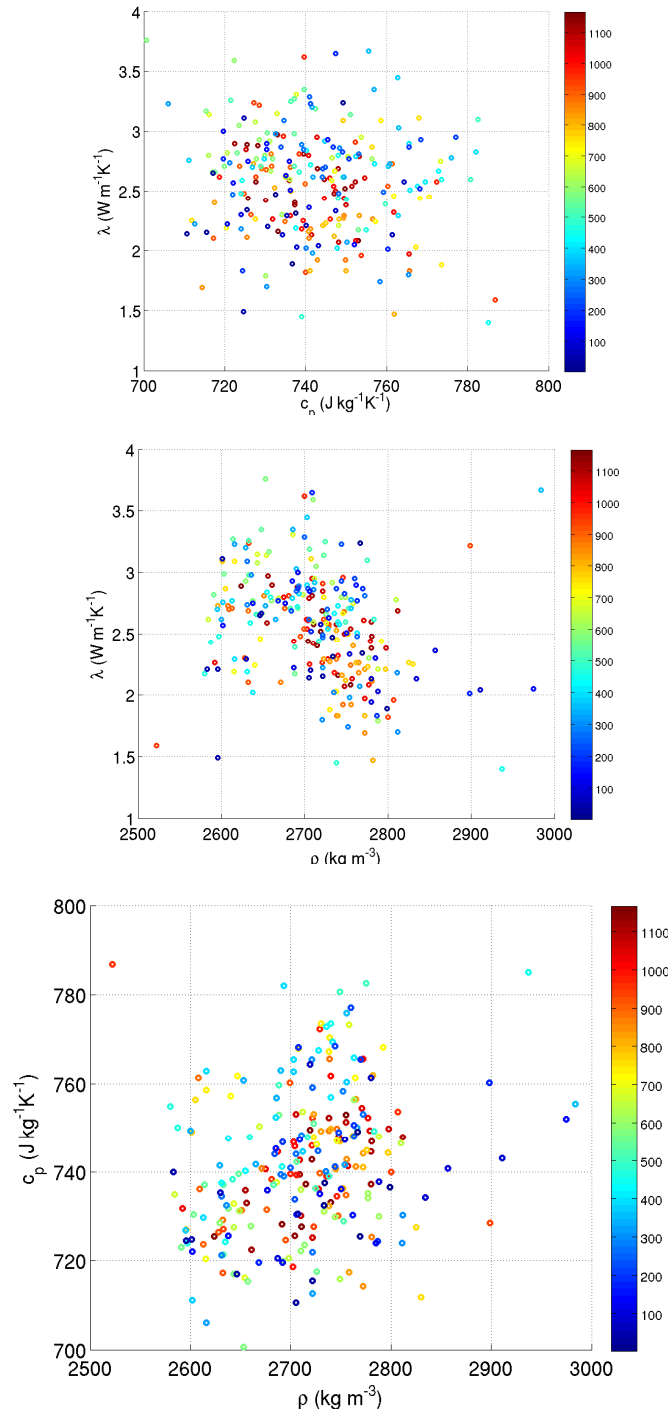


Figure 12. Scatter plots of different rock properties as measured in OL-KR56. Upper left panel: Conductivity vs. specific heat capacity; upper right panel: Conductivity vs. density; Lower panel: Specific heat capacity vs. density. Depth is coded into the color of the symbols. No depth-related clustering is obvious.

The rock porosity is generally very small (<1%) and can be safely neglected. Thus only temperature dependencies of the rock matrix were adopted. For this purpose, the values given in Posiva Oy (2013) were fitted with a function given by Mottaghy et al. (2005) and Mottaghy (2007) (Figure 15).

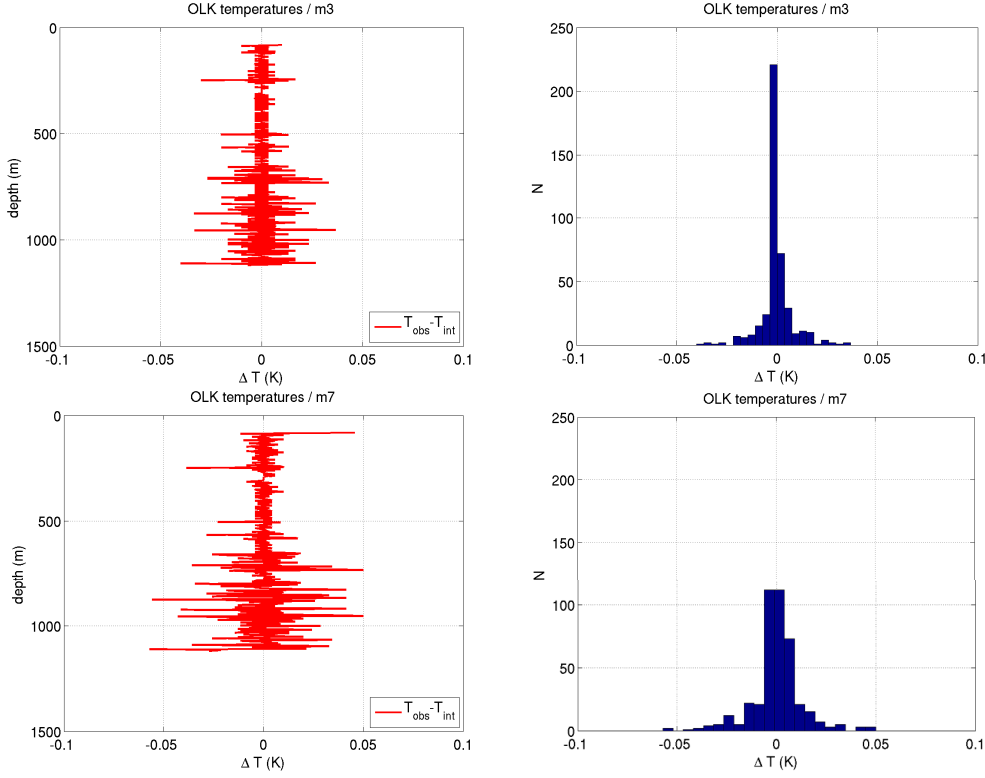


Figure 13. Interpolation of measured temperature data in OL-KR56. Left: residual temperature for 3-point and 7-point moving average, respectively. Right: corresponding histograms. This interpolation was used for the presented results if not indicated otherwise.

For the FD-based forward models, also the basal heat flow density defined as

$$\mathbf{q} = -\lambda \nabla T = -\lambda \frac{\partial T}{\partial z}, \quad (13)$$

has to be imposed at the base of the numerical mesh. Unfortunately, this parameter has a decisive influence on the results of any paleoclimate inversion. In practice it is determined by estimating the temperature gradient over an appropriate depth interval in the drillhole, and the corresponding mean thermal conductivity. However, as demonstrated, e.g. by Rath et al. (2012), the influence of the Last Glacial Cycle (LGC) leads to a downward bias in the top 2000 m. From this we conclude that the estimates determined at shallower depth are still biased downwards. The heat flow densities determined in the near-by drillholes OL-KR40 and OL-KR46 were $40 \pm 1 \text{ mWm}^{-2}$ and $41 \pm 1 \text{ mWm}^{-2}$, respectively (Posiva, 2013). Both values were determined in a depth interval of 100 m between 359 m and 450 m. These values are slightly higher than the ones determined in the deepest borehole OL-KR56, which were determined to be between 37 and 42 mWm^{-2} in the deepest 500 m interval (see Figures 7 - 8 and Table 1). For the inversions shown here, a value of 40 mWm^{-2} was taken as a reasonable value.

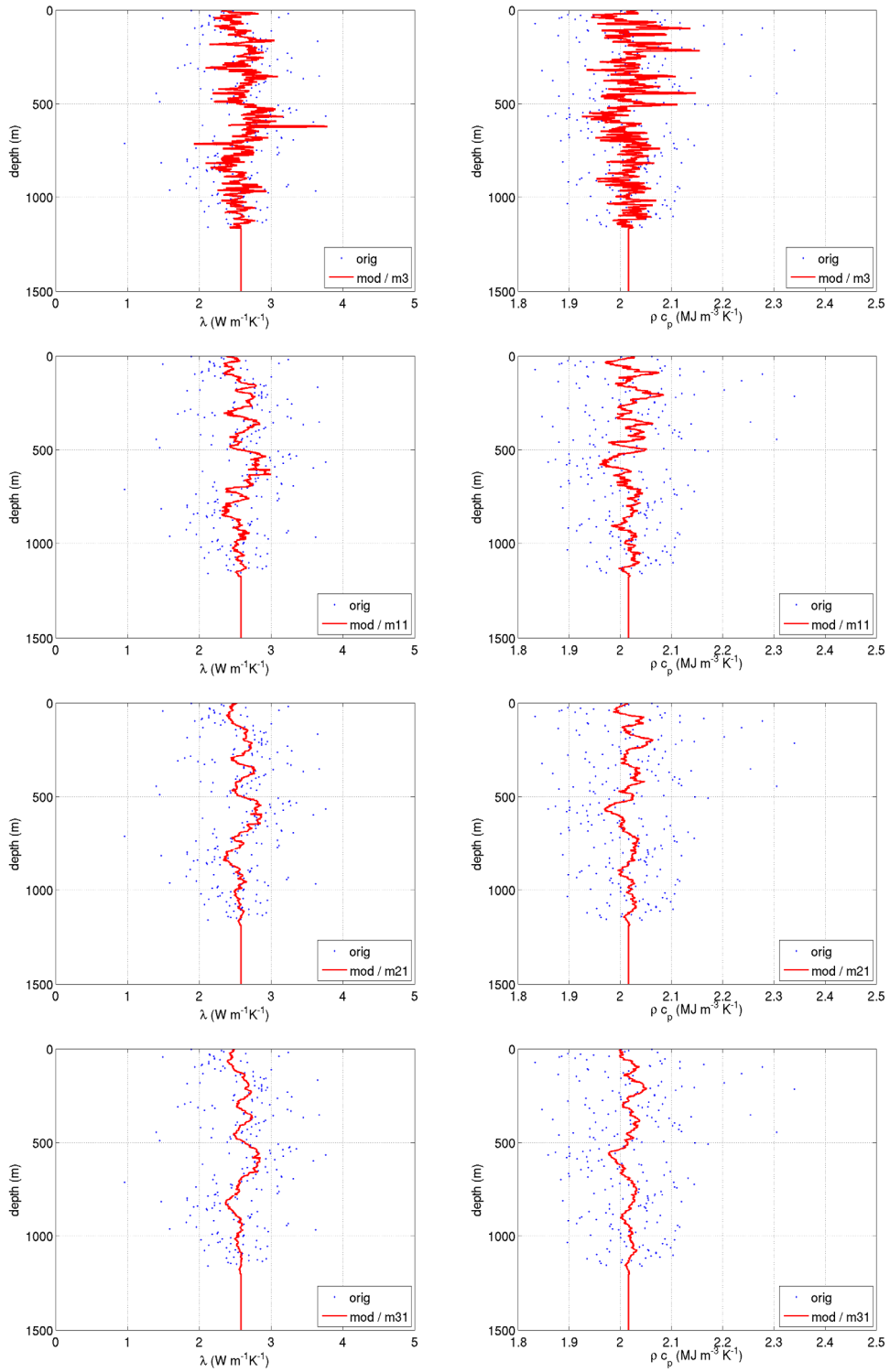


Figure 14. Upscaling of thermal properties in OL-KR56. Left panels: Thermal conductivity; Right panels: Volumetric heat capacity. The length of the averaging operator increases from 5 m in the top panels to 30 m in the lowermost panels.

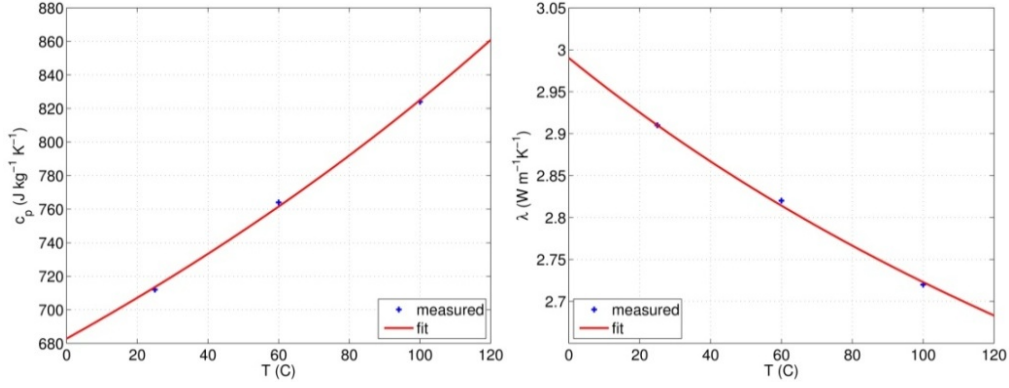


Figure 15. Measured temperature dependencies of Olkiluoto rocks, fitted by the functional relationship given by Mottaghy et al.(2005).

In order to minimize boundary effects, the numerical mesh for the paleoclimate calculations has to extend to at least 4000 m. At this depth a Neumann (i.e., fixed gradient) boundary condition is imposed. Below the depth of the drillhole, the thermal rock properties were set to their global averages, while the heat production term is set to zero. This guarantees that the HDF imposed at 4000 m equals to the one at 1200 m, just below the depth of the drillhole. The related errors in the approximation of the subsurface temperature field in the domain of the drillhole are negligible.

Results

In this section we will not present a single result, but prefer to show a variety of inversion models, which arise from numerical experiments with a large spread of choices in physical setup and/or numerical configuration. The rationale behind this is to identify the robust features of the inversions, which do not depend on a specific approach.

In all cases, the GSTH is parametrized as piecewise constant function, with an logarithmically increasing width of intervals with backward time. This is consistent with the decreasing resolution inherent to the physics of heat conduction. For most cases, the \mathbf{W}_1 regularization with a GCV choice of the optimum weighting parameter τ_1 was used, combined with a fixed small value of τ_0 . Tests have shown that the use of \mathbf{W}_1 or \mathbf{W}_2 does not lead to large differences neither in the resulting models, nor in the data fit (Figure 16).

The observational error was fixed to 0.1 K. It has to be kept in mind that this error does not only include measurement errors, but also any mis-presentations of reality in the forward modeling code. The *RMS* defined by

$$RMS = \sqrt{(N_d - 1)^{-1} \sum_{j=1}^N \left(\frac{T_j^{obs} - T_j^{cal}}{\sigma_j} \right)^2} \quad (14)$$

is <0.5 for all models shown here, indicating that the fit is smaller than the error assumed. Small differences in *RMS* are not considered as significant, as in its

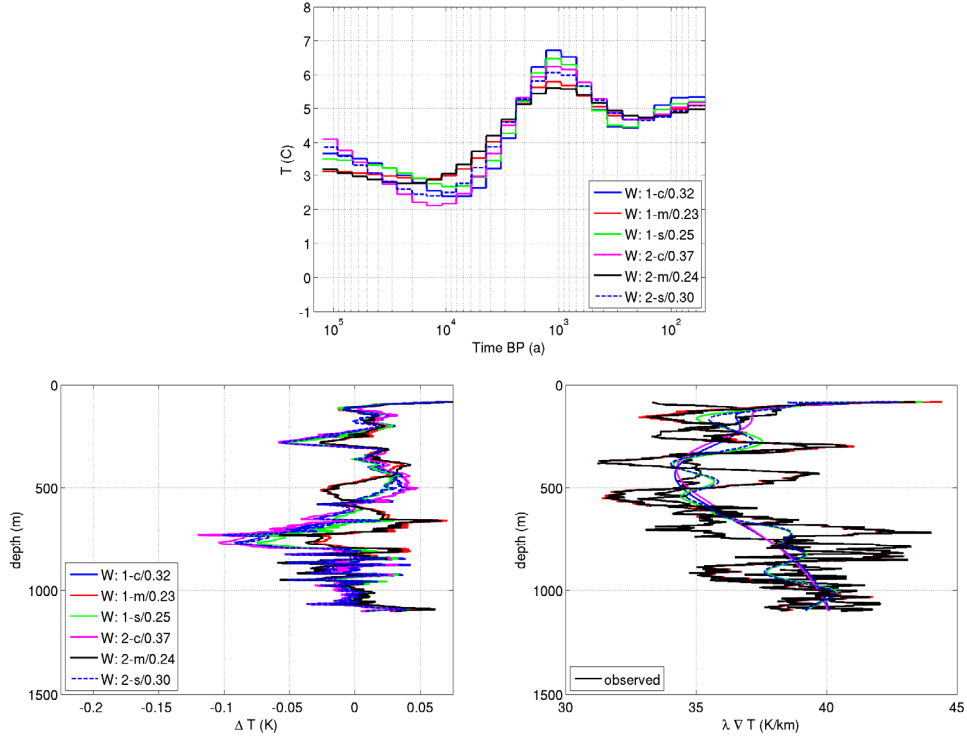


Figure 16. Results for different types of parameter upscaling and different choices of regularization matrices. \mathbf{W}_1 and \mathbf{W}_2 were combined with a small $\mathbf{W}_0 = \tau_0 \mathbf{I}$, ($\tau_0 = 0.003$). A linear vertical mesh was used with different interpolation methods. (c =constant, m =moving average, operator width 17, s =robust smoothing spline, 21 nodes). Top: GSTH estimates; Bottom left: Residuals; Bottom right: HFD.

calculation we did not take into account the influence of the interpolation effect. Usually, an excellent fit with an $\text{RMS} < 0.5$ was obtained after 30 – 50 iterations.

In Figure 18 we present the results for different numbers of intervals M , ranging from 8 to 64 steps. The general form of the resulting GSTHs is very similar, unless the discretization is unreasonably coarse. The case $M=8$ is not able to catch the general structure, though obtaining a low RMS. The stability of the main features of the resulting GSTH indicates not only that the result is robust, but also that the determination of the regularization parameter by GCV is not dependent on the number of steps.

In an additional numerical experiment we investigate the effect of upscaling of the thermophysical parameters on the computational mesh. As already mentioned, the interpolation of the temperature data is not critical, and thus not shown here. Figures 16 and 17 demonstrate the influence of the particular upscaling process. In the former the assumption of constant properties and different methods of smoothing (moving averages or robust splines) are compared. Best results for this case are obtained by a moving average (boxcar or triangle) with an operator width corresponding to about 40 m. Assuming constant properties leads to considerably worse results. This seems to represent a trade-off between trying to follow the small scale structures visible in the measured properties and an averaging necessary to reduce the influence of extreme values (robustness).

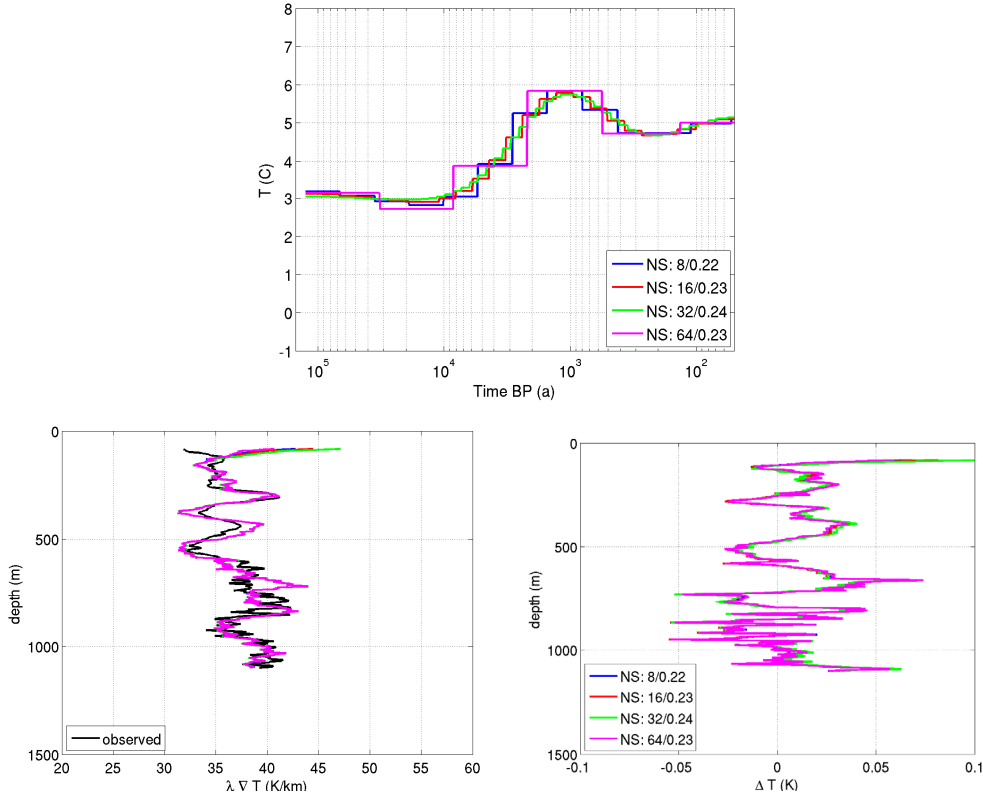


Figure 17. Comparison of results from different parametrization of the inverse model. Here, different numbers of piecewise constant intervals are chosen. All discretizations produce very similar results. The RMS is given after the slash.

The background geothermal heat flow density is by far the most influential parameter. Figure 20 shows the inversion results for different choices of background HFD. For the inversions presented here, we have chosen the value of 40 mWm^{-2} . It is clear that the results are comparable with respect to the data fit, however, the GSTH disagree for times longer than 4 ka BP.

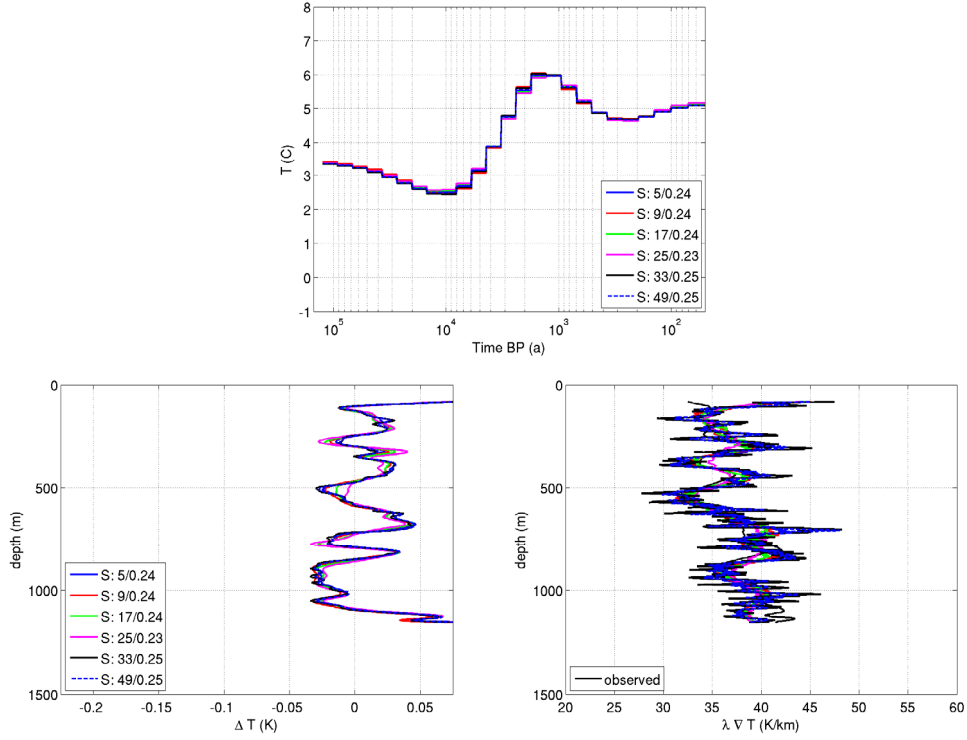


Figure 18. Results for different window lengths used for property smoothing. Top: GSTH estimates for linear and logarithmic vertical meshes and different interpolation methods. In addition to the length of the triangular smoothing operator the RMS is given after the slash.

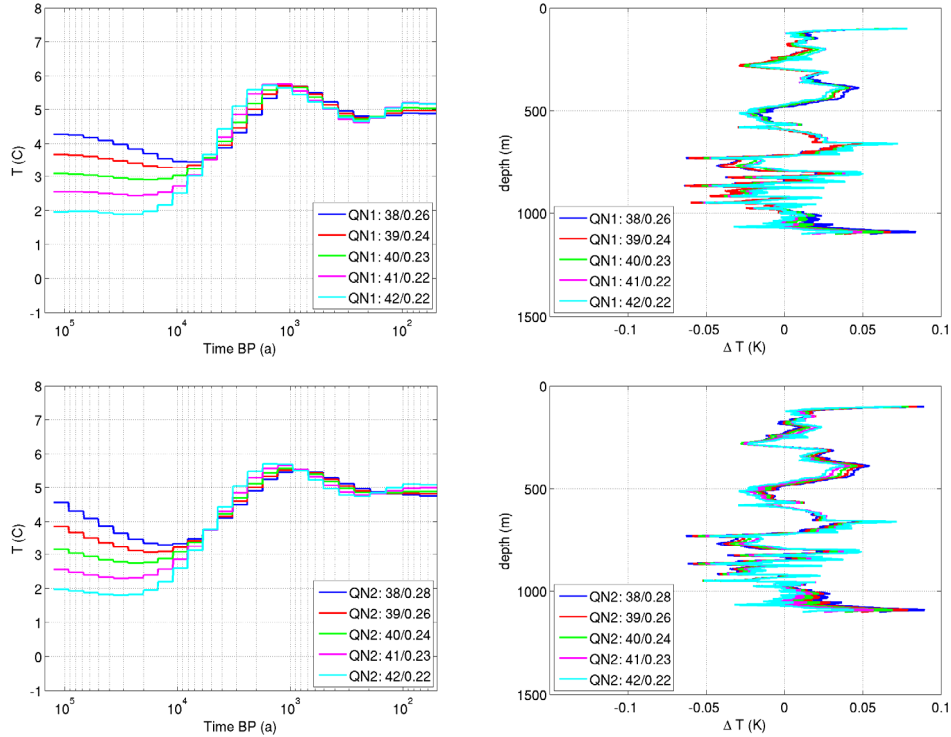


Figure 19. Comparison of results assuming different values of the background HFD. Left: number of temperature steps in parameter vector.

4.3 Nonlinear solution by FD and Bayesian uncertainty evaluation

A Markov Chain Monte Carlo (MCMC) technique was employed to quantify the uncertainty of the GSTH estimates. In particular we used the Metropolis-Hastings algorithm (MH) (Metropolis et al, 1953; Hastings, 1970; Haario et al., 2006). We used the original MH algorithm as implemented by Haario et al. (2006), without any adaptivity, because this led to a premature concentration of models.

There are problems with this choice when dealing with ill-posed inverse problems as the one investigated here. The meaningfulness of the results depends strongly on the reasonable choice of the prior probability density function, which was chosen to be a multidimensional normal distribution $N(m,s)$ characterized by its mean vector m and diagonal covariance matrix C . In particular, we used a result of the variational inversion as a prior (see Figure 18) and a standard deviation σ of 2.5 K for the prior probability density for the GSTH, and 1.5 mWm^{-2} for the basal HFD. The parameters representing the GSTH, however, are not considered independent. Therefore, we introduced a Gaussian temporal covariance matrix defined as

$$C_{i,j}^{\text{gauss}} = \sigma_i^2 \exp \left[\frac{-|i-j|^2}{2L^2} \right] , \quad (15)$$

(see Figure 20). Its width is controlled by a temporal correlation length L of approximately 1/2 of a decade, which agrees with the resolution obtainable in this type of reconstruction (e.g., Demezhko & Schapov, 2001; Demezhko & Gornostaeva, 2015).

A number of chains were started in parallel, each starting from a perturbed version of the prior derived from an estimate of GSTH, assuming a HFD of 40 mWm^{-2} , averaged properties, $M=32$, and a \mathbf{W}_1 regularization as described in Section 4.2.

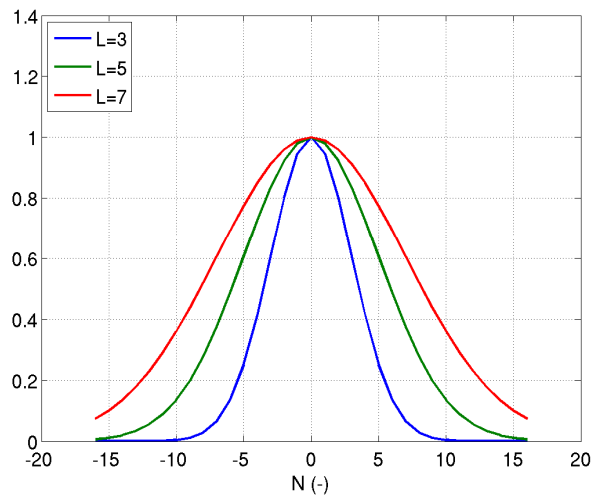


Figure 20. Gaussian temporal covariances. In the MCMC samplings presented in this study, correlation lengths of $7 \cdot \Delta t$ or $5 \cdot \Delta t$ were used.

Results

Results from a MCMC run as described in Section 4.3 are shown in Figure 21. Here the resulting HFD has a median of 40.1 mWm^{-2} , thus reproducing the input, but shows a slight skew to lower values. 68% quantiles are not far from 0.5 K. The residuals for the models in this ensemble lead to an RMS of about 0.21.

In the MCMC inversion the result from the Tikhonov inversion was used as a prior model. The GST values in time periods have been modified in the inversion as shown in Figure 21. The result shown is based on 744,000 samples of which 59 % were accepted by the Monte Carlo algorithm to the posterior distribution. Although the sample number is considerable, the MCMC result may still represent an insufficient number of samples, and the details of the result should not be over-interpreted. The MCMC result shows a similar GSTH as the SVD and Tikhonov inversions, and indicates that the result is stable and represents a true signal in the thermal data of the drill hole.

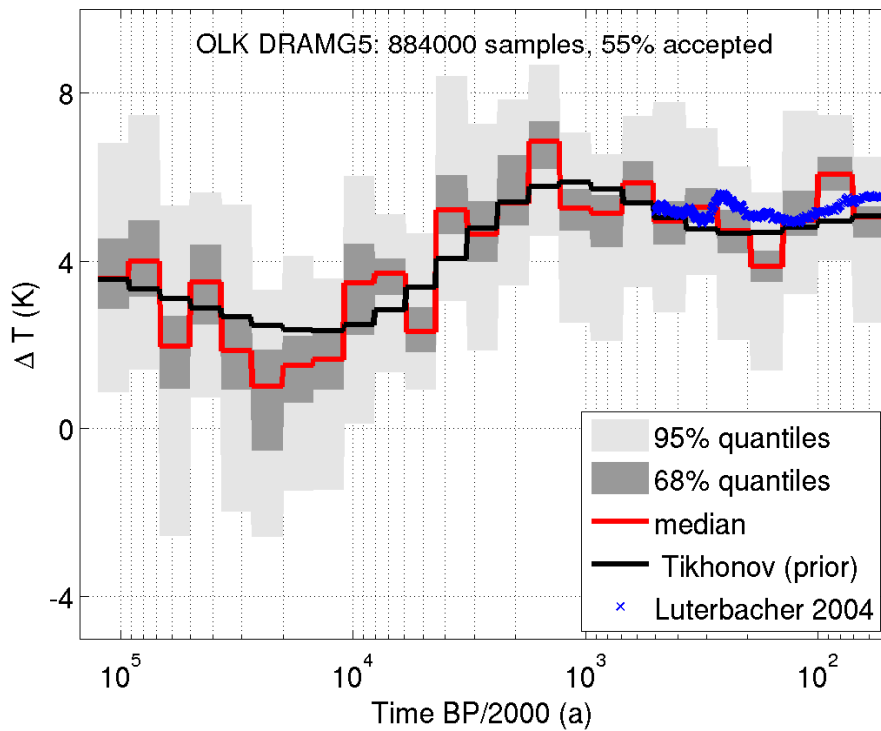


Figure 21. MCMC uncertainty analysis for OL-KR56. In addition to the shading of the 68% and 95% quantiles and the median of the ensemble (red), also the prior GSTH derived from the variational (Tikhonov) inversion is shown. The blue crosses denote a GSTH derived from the Luterbacher et al. (2004) multiproxy reconstruction for the Olkiluoto area. The linear transformation coefficients used are the ones estimated by J. Sundberg (GeoInnova Ab, Sweden, pers. comm. 2014) for the Forsmark area, which shares a comparable climate and vegetation history.

5 DISCUSSION

From the results of the studies represented in the last section, several open questions arise, which will be discussed in this section.

5.1 General considerations

Temperature data in OL-KR56 only reach to a depth of about 1100 m. The depth of the temperature data limits the resolution of the inverse solutions to a few millennia back in time (e.g., Mottaghy, 2005; Clauser, 1999; Kukkonen and Jöeleht, 2003; Kukkonen et al., 2011c), and as argued by Rath et al. (2012), this depth is clearly not enough to resolve the full effect of the glacial cycle. For drillholes shallower than about 1500 m, the inversions are expected to provide a reduced amplitude and smeared shape for the deglaciation signal. Furthermore, the temperature log of OL-KR56 ends at a depth where the curvature of the temperature profile is still relevant (Figure 22).

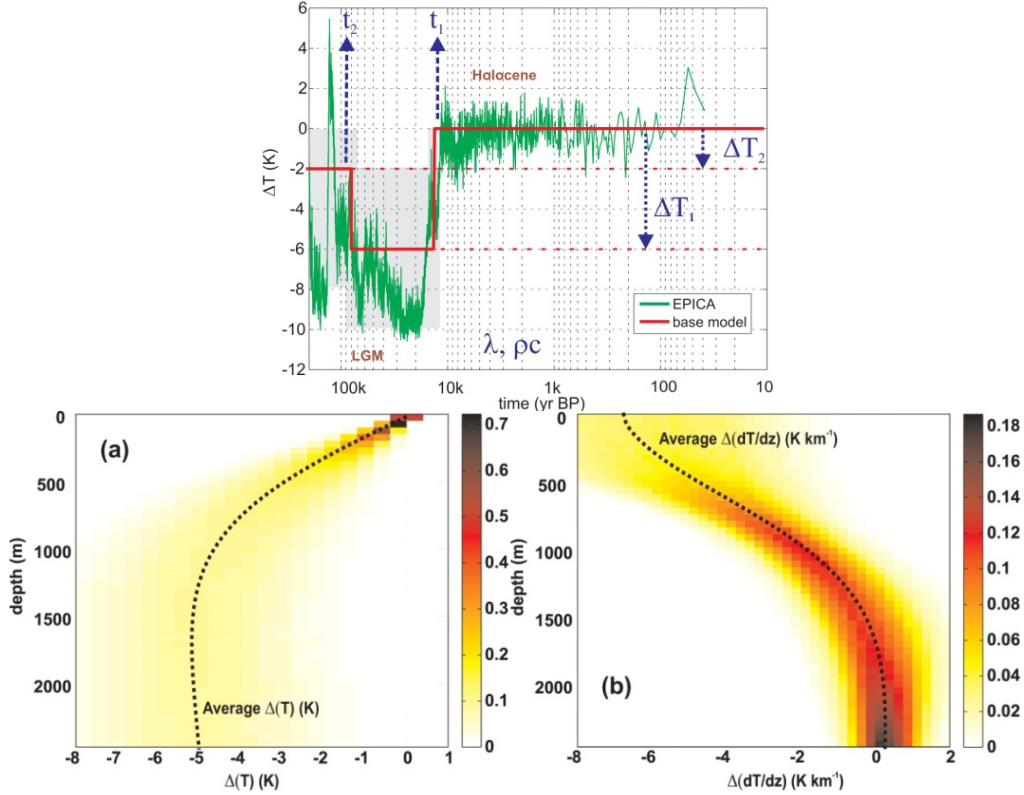


Figure 22. Numerical experiments concerning the signature of the last glacial cycle in drillhole temperature profiles (adapted from Rath et al., 2012). Panels (a) and (b) present the outcome of a Monte Carlo study generating samples with different values for the petrophysical properties and the assumed glacial GSTH (top panel). While (a) is a normalized density plot of the resulting temperature anomaly, (b) shows the vertical gradient of temperature, which is proportional to the heat flow density. EPICA refers to the ice core reconstructions by Jouzel et al. (2007).

In Figure 23, we plotted the sensitivity of the observed data to the discrete values of GSTH near the best model. This means that each curve represents a column of the weighted Jacobian (Equation 11), associated with the corresponding parameter. From this Figure 23 it is quite clear, that the sensitivity to variations dating back from present more than a few millennia is small, and any results for these time periods should be interpreted with care.

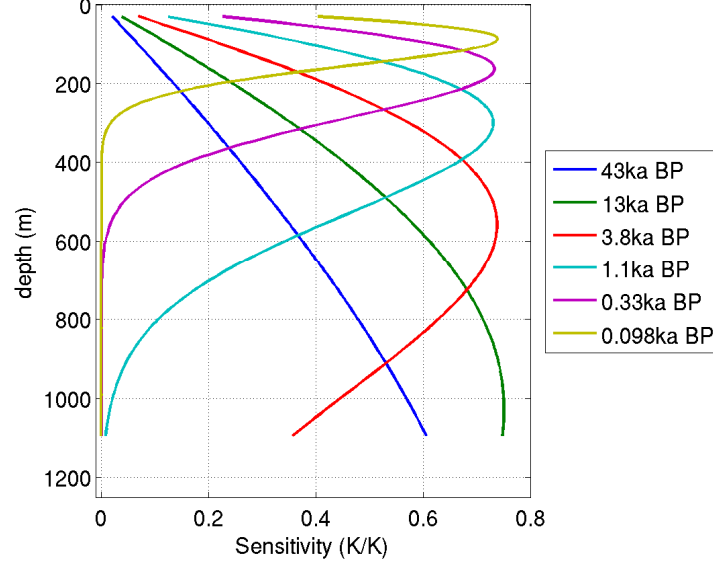


Figure 23. Sensitivities of events centered at different times in the past as a function of depth.

5.2 Physical setup of the forward model

As pointed out by many authors, the simplified 1D inversion applied here produces meaningful results only if none of the assumptions are violated. For the OL-KR56 case, it cannot be excluded that the heterogeneity of thermal properties may have some influence on the results. However, there are reasons to adopt a 1D model as a useful simplification. From the analysis of the measured properties we found that there is no strong layering with respect to the thermal properties, and the contrasts found are associated with a small scale length. This may indicate that there is no necessity to include 3D effects. While the principle of parsimony (“Occam’s razor”) speaks in favour of this simplification, further investigations based on a 3D model may challenge this assumption. Particularly interesting will be the effect of anisotropy, which cannot be treated meaningfully in a 1D environment. However, in crystalline rock as found in Olkiluoto, anisotropy is ambient, and the gneissic rocks show an average anisotropy coefficient of about 1.4 (Kukkonen et al. 2011a).

Related to these problems the representativeness of the laboratory measurements of the thermal rock properties is an important issue. This does not only concern the choice of samples, but it is also significant whether the properties in the lab are identical to the ones under in situ pressure conditions. This may particularly be a problem with the thermal conductivity λ , which is known to be influenced by the presence of micro-

cracks or related phenomena (Hartmann et al., 2005). In the upper 1000 m, this effect may considerably increase the conductivity, thus counteracting the effect of increasing temperature. In the absence of measurements as functions of pressure, we had to neglect this effect. In the present study, thermal conductivity was measured with a divided bar apparatus and a mild pressure (about 0.2 MPa) was applied on the sample along the bar. Moreover, the samples were measured after saturating them for two days in tap water at ambient pressure and temperature (Kukkonen et al. 2011a). The difference between saturated and dry samples of low porosity crystalline rock (Lavia granodiorite) in the divided bar measurement was studied by Ruokonen (1988). Wet samples showed about 4% higher conductivity than dry samples. The OL-KR56 samples have an average effective porosity of 0.44%. We consider that the applied pressure and saturation prior to measurement are sufficient to compensate for the effect of micro-cracks and pores in the present samples.

Another item arises in connection with the forward model. The results of this report show a certain dependence on the upscaling procedure of the petrophysical properties. This procedure is far from unique. Obviously a trade-off has to be found between the adaption to the measured petrophysical properties and the estimated GSTH. Sensitivity experiments in the last section have demonstrated that the choice of the background HFD influences the results strongly for times before 2 ka BP. The younger GSTH, however, appears to be robust with respect to virtually any choices which were made in the formulation of the inverse problem and its parameterization.

The most important physical effect which could possibly interfere with the paleoclimate in the borehole is fluid flow. In OL-KR56, however, no clear indications of thermally relevant fluid flow are found except some local, small-scale effects. At 751-772 m a brittle fault zone is found associated with a small change of temperature gradient, but no permeable structure is known at that depth. Thus we propose that the temperature log can be considered as representing a dominating conductive heat transfer regime, and can be used for inversion.

5.3 Paleoclimatic interpretation

The Fennoscandian area has been exposed to a complicated history of glaciations during the last (Weichselian) glacial cycle. During this period, in the Baltic area, there have been several periods of fast changes in ice sheet extension and thickness. This complicated history only starts being disentangled in the last two decades (Siegert et al., 2001; Andr n et al., 2011, 2012, 2015; Expedition 347 Scientists, 2014) (Figure 24). For Borehole Climatology, the dominating signature in the upper two km is the temperature change related to the deglacial period of the Weichselian cycle. The development of the Baltic area during this period is no less complicated than during the glacial period. After the retreat of the Fennoscandian ice sheet at ≈ 11 ka BP, the Olkiluoto area was covered by water until historical times (≈ 1 ka BP; Karvonen, 2011; Hartley et al., 2012; Smellie et al., 2014).

The development of the relative sea level is reasonably well known from geomorphological indicators, while its salinity is still a matter of discussion, as the different proxy methods do not agree well (Andr n et al., 2011). Salinity affects the

water density minimum, and for the range of salinities considered representative for the Baltic Sea during the Holocene, its value has varied from about 2.5°C (salinity 6 g/L) to about 1°C (salinity 12 g/L) (IOC, SCOR and IAPSO, 2010;). Thus, depending on the water salinity the temperature of the sea floor may have differed considerably from the ground surface temperature on-shore.



Figure 24. Deglacial development of the Baltic (Andrén et al., 2011, 2015). Left: 11.1 ka BP, Yoldia Sea stage. Center: 10.5 ka BP, Ancylus Lake. Right: Littorina Sea stage, about 6.5 ka BP. This is near to the salinity maximum.

When the ice sheet retreated beyond the OL-KR56 site, fresh water from the melting ice sheet was dominant (the Yoldia Sea and Ancylus Lake stages). It was subsequently mixed with saline water, depending on the opening/closing of connections to the North Sea/Atlantic and the reduced freshwater supply. The most saline phase (the Littorina Sea) culminates in the highest relative sea level near 6 ka BP, when the maximum salinity of 12 g/L was reached. This time should also agree with the coldest water in contact with the ground surface. The newer history of the salinity is less clear, as for the last 2 ka there is no agreement on the general trend (Andrén et al., 2011, 2015). Moreover, the salinity deduced from point measurements in the Baltic area show a spatial heterogeneity, and thus may not be valid for a particular location.

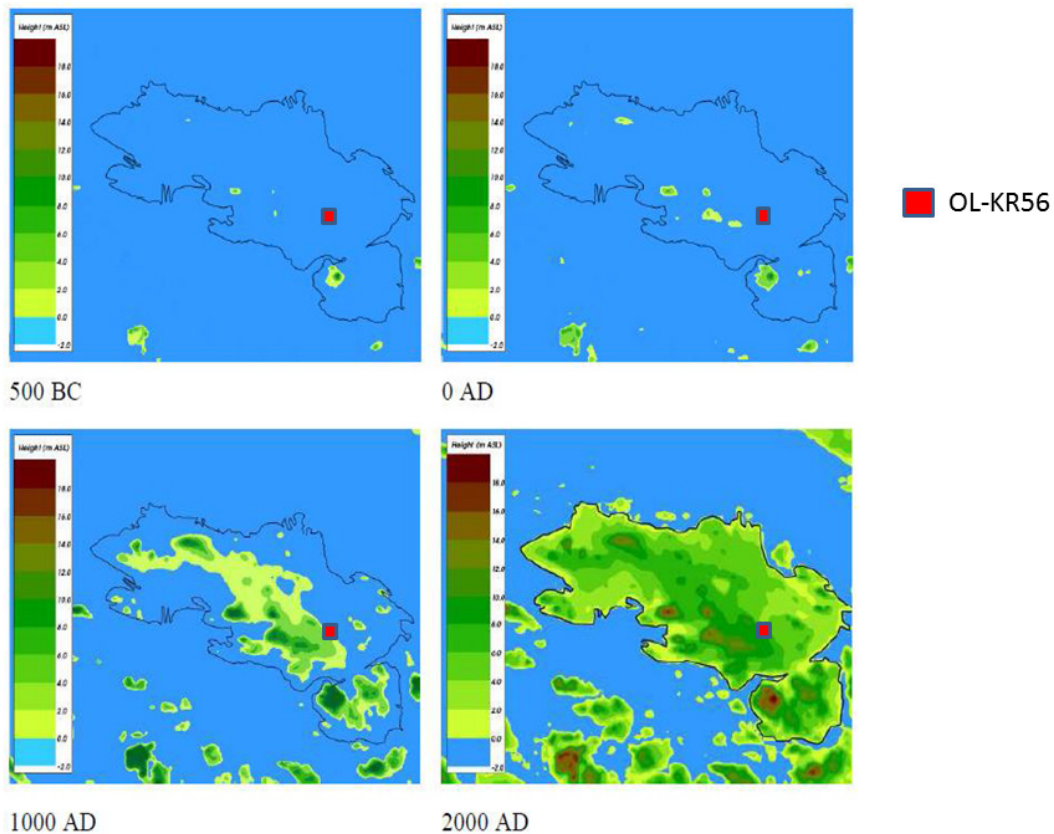


Figure 25. Relative water level in the surroundings of the OL-KR56 site for the last 2000 years (after Hartley et al., 2012).

From the geomorphological indicators, it is highly probable that the OL-KR56 drill site was covered by water until about 1000 a BP (Figure 25). At first sight, this seems to contradict the results obtained here. Indeed, when beginning this project, a working hypothesis was that the atmospheric climate signal for earlier times (e. g., the medieval climate anomaly) would not be visible in the drillhole data. However, the high temperatures between 800 a BP and 2000 a BP appear to be a robust feature of the inversions presented here. The observations allow only conclusions on lower temperatures during the mid-Holocene, while any contributions from the ice sheet cover cannot be deduced, though they are consistent with the data.

The major uncertainties in the inversions influence the shape and amplitude of this feature, but do not challenge its existence. Could there be environmental conditions consistent with the GSTH derived from the drillhole? It has to be kept in mind that the water cover in the area was a very shallow estuarine environment. It has to be expected that salinity, temperature, and hence density may have been influenced by the supply of fresh water from contributing rivers and evaporation/precipitation. Large spatial and temporal gradients in salinities and temperatures probably prevailed (Westman et al., 1999; Boehrer and Schultze, 2008; Valle-Levinson, 2010; Omstedt, 2011). Low winter temperatures at the ground surface may have been inhibited by the isolation and latent heat effects. With these conditions it can not be taken for granted that a stable density

layering existed. It is thus difficult to constrain the drillhole results from independent reconstructions of the conditions of the water cover.

We have compared our results with the paleotemperature reconstructions for the last 500 years published by Luterbacher et al. (2004) (Figures 21 and 26). The lack of agreement between both temperature time series was to be expected. The analysis of drillhole temperatures is not able to retrieve short-term events like the anomaly found between 1700 and 1800 AD, and, together with the smoothing-type regularization, leads only to a strongly filtered signature. The lack of resolution is probably not due to a “smearing” of the signal by groundwater flow. The recent results of Trinchero et al. (2014) indicate that there has not been vigorous vertical fluid flow in the subsurface, as the geochemical characteristics for different generations of groundwater still survive to the current day.

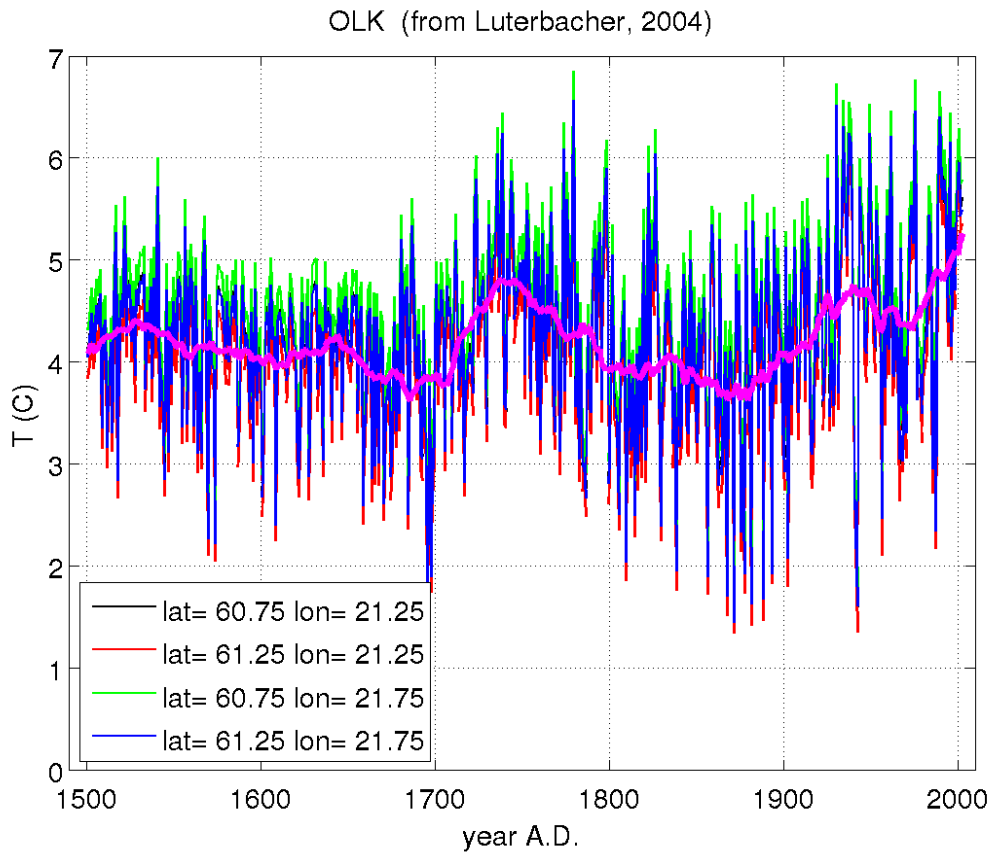


Figure 26. Mean annual air temperature reconstruction for the Olkiluoto site from Luterbacher et al. (2004). Thin lines are the time series for the four nearest points, which were interpolated to the actual position of the drillhole. The thick magenta line represents a 30-year moving average for this site.

Furthermore, the surface air temperature (SAT) reconstructed from a set of proxies for atmospheric conditions as shown in Figure 26 may be considerably different from the GSTH. This is mainly an effect of conditions near the surface, which control the energy and water balance. In the area considered, these factors are dominantly vegetation and snow cover. Their effect is not easily quantified. In some cases, a particular linear SAT-

GST relationship $T_{GST} = a \cdot T_{SAT} + b$ can be derived by a regression between both temperatures involved. However, when applying the relationship derived by Kukkonen (1987) with $a = 0.71$ and $b = 2.93$ to the Olkiluoto site reconstruction, a temperature which is significantly higher than the inverted GSTH is obtained. An analog relation derived for the Forsmark area in Sweden, which shares many climatic similarities with the Olkiluoto site, was estimated by J. Sundberg (GeoInnova Ab, Sweden, pers. comm. 2014). These coefficients $a = 0.59$ and $b = 2.76$ lead to a much better agreement. We are currently not able to say whether this discrepancy is due to the lack of validity of either the linear regression coefficients (which may be wrong due to the local conditions in Olkiluoto), or the multiproxy reconstruction of Luterbacher et al. (2004), which may be biased for this area.

6 CONCLUSIONS

The investigation into the development of past temperature changes in the Olkiluoto area has led to numerous results which can be summarized as follows:

- 1) The main result of the present study is an estimate of the GSTH for the Olkiluoto site based on inverse methods. A pertinent feature is a rather smooth behavior of the GST back to about 800 a BP, preceded by a maximum between 800 a BP and 2500 a BP. These results are robust with respect to discretization of forward model and GSTH, assumed basal heat flow density, and regularization methodology.
- 2) Different methodologies were employed for estimating the GSTH from the drillhole temperature log in OL-KR56. These included both a highly simplified approach based on an analytical solution, as well as a nonlinear numerical approach allowing more complicated physics and a Bayesian uncertainty study based on a Metropolis-Hastings MCMC approach.
- 3) The results presented here depend on the upscaling of rock properties to the quantities usable for the respective inversion technique. Simple averaging leads to a significantly different result than using vertically resolved properties. The upscaling method influences the position and amplitude of the aforementioned temperature maximum.
- 4) The inversions do not yield information on conditions prior to about 2000 a BP, consistent with prior sensitivity estimates, with the exception that temperatures significantly less than modern ones are required. No further conclusions with respect to earlier climate are justified. In particular, it is not justified to conclude on the proposed role of the extended times of water cover in the area.

REFERENCES

- Andrén, T., Björck, S., Andrén, E., Conley, D., Zillén, L. & Anjar J. 2011. The Development of the Baltic Sea Basin During the Last 130 ka. In: Harff, J., Björck, S. & Hoth, P. (Eds.), *The Baltic Sea Basin*, Springer, 75-97.
- Andrén, T., Jørgensen, B.B. & Cotterill, C. 2012. Baltic Sea Basin Paleoenvironment: paleoenvironmental evolution of the Baltic Sea Basin through the last glacial cycle. *IODP Sci. Prosp.*, 10.2204/iodp.sp.347.2012.
- Andrén, T., Jørgensen, B.B., Cotterill, C., Green, S., Andrén, E., Ash, J., Bauersachs, T., Cragg, B., Fanget, A.-S., Fehr, A., Granoszewski, W., Groeneveld, J., Hardisty, D., Herrero-Bervera, E., Hyttinen, O., Jensen, J.B., Johnson, S., Kenzler, M., Kotilainen, A., Kotthoff, U., Marshall, I.P.G., Martin, E., Obrochta, S., Passchier, S., Quintana-Krupinski, N., Riedinger, N., Slomp, C., Snowball, I., Stepanova, A., Strano, S., Torti, A., Warnock, J., Xiao, N., & Zhang, R. 2015. Expedition 347 summary. *Proc. IODP*, 347, doi:10.2204/iodp.proc.347.101.2015
- Aster, R., Borchers, B. & Thurber, C. 2013. *Parameter estimation and inverse problems*. Academic Press, San Diego CA, USA, 360 pp.
- Beck, A.E. 1977. Climatically perturbed temperature gradients and their effect on regional and continental heat flow means. *Tectonophysics*, 41, 17-39.
- Beltrami, H. & Mareschal, J.-C. 1992. Ground surface temperature histories for central and eastern Canada from geothermal measurements: Little Ice Age signature. *Geophys. Res. Lett.*, 19, 689-692.
- Beltrami, H., Cheng, L. & Mareschal, J.C. 1997. Simultaneous inversion of borehole temperature data for determination of ground temperature history. *Geophys. J. Int.*, 129, 311-318.
- Benfield, A.E. 1949. Terrestrial heat flow in Britain. *Proceedings of the Royal Society A, Mathematical, Physical and Engineering Sciences*, 173, 428-450.
- Birch, F. 1948. The effects of Pleistocene climatic variations upon geothermal gradients. *American Journal of Science*, 246, 729-760.
- Bodri, L. & Cermak, V. 2007. *Borehole climatology: a new method how to reconstruct climate*. Elsevier, Oxford-Amsterdam, 335 pp.
- Bohrer, B. & Schultze, M. 2008. Stratification of lakes. *Rev. Geophys.*, 46, 2006RG0002010, doi:10.1029/2006RG000210, 27pp.
- Brynjarsdottir, J. & Berliner, L. M. 2011. Bayesian hierarchical modeling for temperature reconstruction from geothermal data. *Ann. Appl. Stat.*, 5, 1328-1359.
- Carslaw, H. S. & Jaeger, J. C. 1959. *Conduction of heat in solids* Oxford University Press, Oxford, UK, 510 pp.

Clauser, C., 1999. Thermal signatures of heat transfer processes in the Earth's crust. Lecture Notes in Earth Sciences, Vol. 85, ISBN 3-540-65604-9, Springer Verlag, Heidelberg-Berlin, 111p.

Demezhko, D. Y. & Shchapov, V. A. 2001. 80,000 years ground surface temperature history inferred from the temperature depth log measured in the superdeep hole SG-4 (the Urals, Russia) *Global and Planetary Change*, 29, 219-230.

Demezhko, D. Y. & Gornostaeva, A. A. 2015. Late Pleistocene-Holocene ground surface heat flux changes reconstructed from borehole temperature data (the Urals, Russia). *Climate of the Past*, 11, 647-652.

Drury, M. J. 1984. Borehole temperature logging for the detection of water flow. *Ge exploration*, 22, 231-243.

Expedition 347 Scientists 2014. Baltic Sea Basin Paleoenvironment. Paleoenvironmental evolution of the Baltic Sea Basin through the last glacial cycle. IODP Prel. Rep., 10.2204/iodp.pr.347.2014.

Farquharson, C. G. & Oldenburg, D. W. 2004. A comparison of automatic techniques for estimating the regularization parameter in non-linear inverse problems. *Geophys. J. Int.*, 156, 411-425.

González-Rouco, J. F., Beltrami, H., Zorita, E. & Stevens, M. B. 2009. Borehole climatology: a discussion based on contributions from climate modeling. *Climate of the Past*, 2009, 4, 1-80.

Haario, H., Laine, M., Mira, A. & Saksman, E. 2006. DRAM: Efficient adaptive MCMC. *Statistics and Computing*, 16, 339-354.

Hadamard, J., 1923. Lectures on the Cauchy Problem in Linear Partial Differential Equations. Yale University Press, New Haven CT, 316 p.

Hansen, P. C. 1998. Rank Deficient and Discrete Ill-Posed Problems. SIAM, Philadelphia, PA, USA, 243 pp.

Hansen, P. C. 2010. Discrete Inverse Problems. Insight and Algorithms. SIAM, Philadelphia PA, USA, 206 pp.

Hartley, L., Appleyard P., Baxter, S., Hoek, J., Roberts, D., & Swan, D. 2012. Development of a Hydrogeological Discrete Fracture Network Model of Olkiluoto; Site Descriptive Model 2011. Working Report 2012-32. Posiva Oy, Eurajoki. 540 pp.

Hartmann, A. 2008. Inversion of geothermal parameters using borehole and core data, PhD thesis, RWTH Aachen University, 127 pp.

Hartmann, A., Rath, V. & Clauser, C. 2005. Thermal conductivity from core and well log data. *Int. J. Rock Mech. & Min. Sci.*, 42, 1042-1055.

Hastings, W. K. 1970. Monte Carlo sampling methods using Markov chains and their applications. *Biometrika*, 57, 97-109.

IOC, SCOR & IAPSO 2010: The international thermodynamic equation of seawater – 2010: Calculation and use of thermodynamic properties. Intergovernmental Oceanographic Commission, Manuals and Guides No. 56, UNESCO (English), 196 pp.

Jessop, A.M. 1971. The distribution of glacial perturbation of heat flow in Canada. *Canadian Journal of Earth Sciences*, 8, 162-166.

Jouzel, J., Masson-Delmotte, V., Cattani, O., Dreyfus, G., Falourd, S., Hoffmann, G., Minster, B., Nouet, J., Barnola, J., Chappellaz, J., Fischer, H., Gallet, J., Johnsen, S., Leuenberger, M., Loulergue, L., Luethi, D., Oerter, H., Parrenin, F., Raisbeck, G., Raynaud, D., Schilt, A., Schwander, J., Selmo, E., Souchez, R., Spahni, R., Stauffer, B., Steffensen, J., Stenni, B., Stocker, T., Tison, J., Werner, M., and Wolff, E.: Orbital and Millennial Antarctic Climate Variability over the Past 800,000 Years, *Science*, 317, 793–797, 2007.

Karvonen, T. 2011. Olkiluoto Surface and Near-Surface Hydrological Modelling in 2010, Working Report 2011-50, Posiva Oy, Eurajoki. 156 pp.

Kukkonen, I. 1987. Vertical variation of apparent and palaeoclimatically corrected heat flow densities in the central Baltic Shield. *Journal of Geodynamics*, 8, 33-53.

Kukkonen, I.T. & Jöeleht 2003. Weichselian temperatures from geothermal heat flow data. *Journal of Geophysical Research*, 108 (B3), ETG-9, 11 pp.

Kukkonen, I. T. & Peltoniemi, S. 1998. Relationships between thermal and other petrophysical properties of rocks in Finland. *Phys. Chem. Earth*, 23, 341-349.

Kukkonen, I.T. & Šafanda, J. 1996. Palaeoclimate and structure: the most important factors controlling subsurface temperatures in crystalline rocks. A case history from Outokumpu, eastern Finland. *Geophysical Journal International*, 126, 101-112.

Kukkonen, I., Korpisalo, A. & Koskinen, T. 2011b. Inverse Temperature Gradient Method for Estimating Thermal Conductivity in Drillholes. Posiva Oy, Working Report 2011-79, 30 p.

Kukkonen, I., Korpisalo, A., Suppala, I., & Koskinen, T. 2014. In situ determination of thermal properties of rocks in crystalline rock drill holes with TERO56 and TERO76 devices. Posiva Oy, Report 2013-06, 56 p.

Kukkonen, I., Kivekäs, L., Vuoriainen, S. & Kääriä, M. 2011a. Thermal Properties of Rocks in Olkiluoto: Results of Laboratory Measurements 1994–2010. Posiva Working Report, 2011-17, 96 p.

Kukkonen, I. T., Rath, V., Kivekäs, L., Šafanda, J. & Čermak, V. 2011c. Geothermal Studies of the Outokumpu Deep Drill Hole, Finland: Vertical variation in heat flow and paleoclimatic implications. *Physics of the Earth and Planetary Interiors*, 188, 9-25.

- Lewis, T.J. & Beck, A.E. 1977. Analysis of heat flow data – detailed observations in many holes in a small area. *Tectonophysics*, 41, 41 – 59.
- Lanczos, C. 1961. *Linear Differential Operators*. Van Nostrand, Amsterdam NL, 580 pp.
- Luterbacher, J., Dietrich, D., Xoplaki, E. Grosjean, M. & Wanner, H. 2004. European seasonal and annual temperature variability, trends and extremes since 1500. *Science*, 303, 1499-1503.
- Mareschal, J.-C., Rolandone, F. and Bienfait, G. 1999. Heat flow variations in a deep borehole near Sept-Iles, Quebec, Canada: Palaeoclimatic interpretation and implications for regional heat flow estimates. *Geophys. Res. Lett.*, 26, 2049-2052.
- Metropolis, N., Rosenbluth, A. W., Rosenbluth, M. N., Teller, A. H. & Teller, E. 1953. Equations of State Calculations by Fast Computing Machines. *J. Chem. Physics*, 1953, 21, 1087-1092.
- Mosegaard, K. & Tarantola, A. 1995. Monte-Carlo Sampling of Solutions to Inverse Problems. *J. Geophys. Res.*, 100, 12431-12447.
- Mosegaard, K. & Tarantola, A. 2002. Probabilistic Approach to Inverse Problems. *International Handbook of Earthquake and Engineering Seismology, Part A*, Academic Press, San Diego CA, 237-265.
- Mottaghy, D., Popov, Y. A., Schellschmidt, R., Clauser, C., Kukkonen, I. T., Nover, G., Milanovsky, S. & Romushkevich, R. A. 2005. New heat flow data from the immediate vicinity of the Kola superdeep borehole: Vertical variation in heat flow density confirmed. *Tectonophysics*, 401, 119-142.
- Mottaghy, D. & Rath, V. 2006. Latent heat effects in subsurface heat transport modeling and their impact on paleotemperature reconstructions. *Geophys. J. Int.*, 164, 236-245.
- Mottaghy, D. 2007. Heat transfer processes in the upper crust: influence of structure, fluid flow, and palaeoclimate. PhD thesis, RWTH Aachen University, 97 p.
- Omstedt, A. 2011. *Guide to Process Based Modeling of Lakes and Coastal Seas*. Springer, Berlin-Heidelberg, Germany, 288 p.
- Posiva Oy 2013. Olkiluoto Site Description 2011, Report POSIVA 2011-02, Posiva Oy, Eurajoki, Finland, 815 p.
- Rath, V., González-Rouco, J. F. & Goosse, H. 2012. Impact of postglacial warming on borehole reconstructions of last millennium temperatures. *Climate of the Past*, 8, 1059-1066.
- Rath, V. & Mottaghy, D., 2007. Smooth inversion for ground surface temperature histories: estimating the optimum regularization parameter by generalized cross-validation. *Geophys. J. Int.*, 171, 1440-1448.

- Ripatti, K, Komulainen, J. & Pöllänen, J., 2014. Difference Flow and Electrical Conductivity Measurements at the Olkiluoto Site in Eurajoki, Drillholes OL-KR56, OL-KR57 and OL-KR57B. Posiva Oy, Working Report, 2013-26, 176 p.
- Ruokonen, J. 1988. Petrophysical study on rock porosity of the Lavia test hole drill core, Finland. Unpublished Master's thesis, Helsinki University of Technology, 80 p + 26 p. app. (in Finnish).
- Shen, P.Y. and Beck, A.E. 1991. Least squares inversion of borehole temperature measurements in functional space. *J. Geophys. Res.*, 96, 19965-19979.
- Siegert, M. J., Dowdeswell, J. A., Hald, M. & Svendsen, J.-I. 2001. Modelling the Eurasian Ice Sheet through a full Weichselian glacial cycle. *Global and Planetary Change*, 31, 367-385.
- Smellie, J. (ed.), Pitkänen, P., Koskinen, L., Aaltonen, I., Eichinger, F., Waber, N., Sahlstedt, E., Siitari-Kauppi, M., Karhu, J., Löfman J. , Poteri, A. 2014. Evolution of the Olkiluoto site: Palaeohydrogeochemical considerations, Posiva Oy, Working Report 2014-27, 228 p.
- Tarantola, A. 2005. *Inverse Problem Theory and Methods for Model Parameter Estimation*, SIAM, Philadelphia PA, 339 p.
- Toropainen, V., 2012. Core Drilling of Deep Drillhole OL-KR56 at Olkiluoto in Eurajoki 2011–2012. Posiva Oy, Working Report, 2013-26, 212 p.
- Trinchero, P.; Delos, A.; Molinero, J.; Dentz, M. & Pitkänen, P., 2014. Understanding and modelling dissolved gas transport in the bedrock of three Fennoscandian sites. *J. Hydrol.*, 3, 10.1016/j.jhydrol.2014.03.011.
- Valle-Levinson, A. (Ed.) 2010. *Contemporary issues in estuarine physics*. Cambridge University Press, New York, USA, 315 p.
- Vogel, C. R. 2002. *Computational Methods for Inverse Problems*, SIAM, Philadelphia PA, USA, 179 p.
- Wahba, G. 1990. *Spline Models for Observational Data*. SIAM, Philadelphia PA, USA, 161 p.
- Westman, P., Stefan Wastegard, K. S., Gustafsson, B. & Omstedt, A. 1999. Salinity change in the Baltic Sea during the last 8,500 years: evidence, causes and models. *SKB TR-99-38*, 52 p.

APPENDICES**Appendix 1: Temperature data in OL-KR56**

Appendix 1. Temperature data in OL-KR56

Logging depth [m]	Vertical depth [m]	Temperature [°C]	Logging depth [m]	Vertical depth [m]	Temperature [°C]	Logging depth [m]	Vertical depth [m]	Temperature [°C]	Logging depth [m]	Vertical depth [m]	Temperature [°C]
2.50	2.49	3.890	80.11	78.84	6.210	157.71	154.66	7.263	235.32	230.45	8.299
5.01	4.98	5.402	82.61	81.29	6.228	160.22	157.11	7.295	237.82	232.89	8.332
7.51	7.47	5.931	85.11	83.73	6.261	162.72	159.55	7.328	240.32	235.32	8.367
10.01	9.95	6.224	87.62	86.19	6.311	165.22	161.99	7.362	242.83	237.77	8.391
12.52	12.45	6.378	90.12	88.63	6.332	167.73	164.45	7.394	245.33	240.21	8.421
15.02	14.92	6.449	92.62	91.07	6.353	170.23	166.89	7.430	247.83	242.65	8.454
17.52	17.40	6.467	95.13	93.53	6.377	172.73	169.33	7.469	250.34	245.10	8.483
20.03	19.88	6.387	97.63	95.97	6.421	175.24	171.78	7.496	252.84	247.54	8.565
22.53	22.35	6.314	100.13	98.41	6.450	177.74	174.23	7.519	255.34	249.98	8.552
25.03	24.81	6.264	102.64	100.87	6.495	180.24	176.67	7.562	257.85	252.43	8.583
27.54	27.28	6.221	105.14	103.31	6.520	182.75	179.12	7.598	260.35	254.86	8.615
30.04	29.74	6.183	107.64	105.75	6.555	185.25	181.56	7.633	262.85	257.30	8.647
32.54	32.20	6.152	110.15	108.20	6.577	187.75	184.00	7.664	265.36	259.75	8.674
35.05	34.66	6.125	112.65	110.65	6.619	190.26	186.46	7.701	267.86	262.19	8.709
37.55	37.11	6.099	115.15	113.09	6.640	192.76	188.90	7.743	270.36	264.62	8.743
40.05	39.57	6.067	117.66	115.54	6.680	195.26	191.34	7.778	272.87	267.07	8.769
42.56	42.03	6.039	120.16	117.98	6.729	197.77	193.79	7.814	275.37	269.51	8.798
45.06	44.48	6.013	122.66	120.42	6.754	200.27	196.23	7.846	277.87	271.95	8.830
47.56	46.94	6.004	125.17	122.87	6.794	202.77	198.68	7.886	280.38	274.39	8.861
50.07	49.40	6.000	127.67	125.31	6.834	205.28	201.13	7.920	282.88	276.83	8.890
52.57	51.85	6.004	130.17	127.75	6.872	207.78	203.57	7.950	285.38	279.27	8.924
55.07	54.30	6.013	132.68	130.20	6.910	210.28	206.01	7.986	287.89	281.71	8.957
57.58	56.76	6.020	135.18	132.65	6.945	212.79	208.46	8.011	290.39	284.15	8.993
60.08	59.22	6.031	137.68	135.09	6.980	215.29	210.90	8.051	292.89	286.59	9.032
62.58	61.67	6.052	140.19	137.54	7.014	217.79	213.34	8.079	295.40	289.03	9.069
65.09	64.13	6.074	142.69	139.98	7.053	220.30	215.79	8.114	297.90	291.47	9.108
67.59	66.58	6.088	145.19	142.43	7.092	222.80	218.23	8.141	300.40	293.91	9.151
70.09	69.03	6.104	147.70	144.88	7.134	225.30	220.67	8.173	302.91	296.35	9.188
72.60	71.48	6.139	150.20	147.32	7.166	227.81	223.12	8.210	305.41	298.79	9.227
75.10	73.93	6.164	152.71	149.77	7.198	230.31	225.56	8.234	307.91	301.23	9.270
77.60	76.38	6.182	155.21	152.21	7.230	232.81	228.00	8.270	310.42	303.67	9.310

Appendix 1. Temperature data in OL-KR56 (cont.)

Logging depth [m]	Vertical depth [m]	Temperature [°C]	Logging depth [m]	Vertical depth [m]	Temperature [°C]	Logging depth [m]	Vertical depth [m]	Temperature [°C]	Logging depth [m]	Vertical depth [m]	Temperature [°C]
312.92	306.11	9.351	390.52	381.67	10.370	468.13	457.20	11.380	545.73	532.69	12.376
315.42	308.54	9.390	393.03	384.11	10.404	470.63	459.63	11.412	548.24	535.13	12.409
317.93	310.99	9.431	395.53	386.55	10.435	473.14	462.07	11.444	550.74	537.56	12.440
320.43	313.42	9.468	398.03	388.98	10.467	475.64	464.50	11.475	553.24	539.99	12.473
322.93	315.86	9.500	400.54	391.42	10.496	478.14	466.94	11.509	555.75	542.43	12.502
325.44	318.31	9.534	403.04	393.86	10.528	480.65	469.38	11.541	558.25	544.87	12.533
327.94	320.74	9.565	405.54	396.29	10.558	483.15	471.81	11.575	560.75	547.30	12.564
330.44	323.17	9.598	408.05	398.73	10.592	485.65	474.24	11.607	563.26	549.74	12.595
332.95	325.62	9.628	410.55	401.17	10.621	488.16	476.69	11.636	565.76	552.17	12.625
335.45	328.05	9.662	413.05	403.60	10.657	490.66	479.12	11.669	568.26	554.60	12.657
337.95	330.49	9.693	415.56	406.04	10.689	493.16	481.55	11.700	570.77	557.04	12.691
340.46	332.93	9.725	418.06	408.47	10.723	495.67	483.99	11.732	573.27	559.47	12.724
342.96	335.37	9.755	420.56	410.91	10.753	498.17	486.42	11.766	575.77	561.90	12.754
345.46	337.80	9.785	423.07	413.35	10.789	500.67	488.86	11.798	578.28	564.34	12.817
347.97	340.25	9.817	425.57	415.78	10.819	503.18	491.30	11.833	580.78	566.77	12.827
350.47	342.68	9.852	428.07	418.22	10.852	505.68	493.73	11.864	583.28	569.20	12.848
352.97	345.11	9.884	430.58	420.66	10.886	508.18	496.16	11.896	585.79	571.64	12.880
355.48	347.56	9.915	433.08	423.09	10.921	510.69	498.60	11.929	588.29	574.08	12.908
357.98	349.99	9.948	435.58	425.52	10.953	513.19	501.04	11.959	590.79	576.51	12.930
360.48	352.43	9.979	438.09	427.97	10.989	515.69	503.47	12.024	593.30	578.95	12.952
362.99	354.87	10.005	440.59	430.40	11.021	518.20	505.91	12.020	595.80	581.38	12.976
365.49	357.30	10.038	443.09	432.83	11.058	520.70	508.34	12.057	598.30	583.81	13.037
367.99	359.74	10.065	445.60	435.27	11.091	523.20	510.77	12.088	600.81	586.25	13.073
370.50	362.18	10.099	448.10	437.71	11.124	525.71	513.22	12.122	603.31	588.68	13.105
373.00	364.61	10.129	450.61	440.15	11.157	528.21	515.65	12.154	605.81	591.11	13.141
375.50	367.05	10.172	453.11	442.58	11.189	530.71	518.08	12.187	608.32	593.55	13.171
378.01	369.49	10.202	455.61	445.01	11.220	533.22	520.52	12.220	610.82	595.98	13.206
380.51	371.93	10.233	458.12	447.46	11.253	535.72	522.95	12.250	613.32	598.41	13.236
383.01	374.36	10.269	460.62	449.89	11.283	538.22	525.38	12.281	615.83	600.85	13.272
385.52	376.80	10.301	463.12	452.32	11.315	540.73	527.83	12.312	618.33	603.28	13.305
388.02	379.24	10.338	465.63	454.76	11.346	543.23	530.26	12.343	620.83	605.71	13.337

Appendix 1. Temperature data in OL-KR56 (cont.)

Logging depth [m]	Vertical depth [m]	Temperature [°C]	Logging depth [m]	Vertical depth [m]	Temperature [°C]	Logging depth [m]	Vertical depth [m]	Temperature [°C]	Logging depth [m]	Vertical depth [m]	Temperature [°C]
623.34	608.15	13.369	700.94	683.51	14.382	778.55	758.81	15.419	856.15	834.01	16.620
625.84	610.58	13.399	703.44	685.93	14.410	781.05	761.24	15.449	858.65	836.43	16.658
628.34	613.01	13.433	705.95	688.37	14.454	783.55	763.66	15.483	861.16	838.86	16.694
630.85	615.45	13.468	708.45	690.79	14.493	786.06	766.10	15.517	863.66	841.28	16.732
633.35	617.88	13.499	710.95	693.22	14.527	788.56	768.52	15.552	866.16	843.70	16.773
635.85	620.30	13.532	713.46	695.66	14.532	791.06	770.95	15.588	868.67	846.13	16.843
638.36	622.74	13.559	715.96	698.08	14.584	793.57	773.38	15.629	871.17	848.55	16.870
640.86	625.17	13.591	718.46	700.51	14.612	796.07	775.81	15.665	873.67	850.97	16.887
643.36	627.60	13.623	720.97	702.94	14.638	798.57	778.23	15.706	876.18	853.40	16.889
645.87	630.04	13.656	723.47	705.37	14.681	801.08	780.67	15.746	878.68	855.81	16.908
648.37	632.47	13.688	725.97	707.80	14.750	803.58	783.09	15.786	881.18	858.23	16.991
650.87	634.90	13.720	728.48	710.23	14.740	806.08	785.52	15.825	883.69	860.66	17.018
653.38	637.33	13.751	730.98	712.66	14.798	808.59	787.95	15.864	886.19	863.08	17.034
655.88	639.76	13.782	733.48	715.09	14.784	811.09	790.37	15.907	888.69	865.50	17.051
658.38	642.19	13.815	735.99	717.52	14.848	813.59	792.80	15.945	891.20	867.92	17.068
660.89	644.63	13.848	738.49	719.95	14.886	816.10	795.23	15.981	893.70	870.34	17.139
663.39	647.05	13.880	740.99	722.37	14.887	818.60	797.65	16.030	896.20	872.76	17.184
665.89	649.48	13.912	743.50	724.81	14.926	821.10	800.07	16.119	898.71	875.19	17.287
668.40	651.92	13.945	746.00	727.23	14.936	823.61	802.51	16.154	901.21	877.60	17.304
670.90	654.34	13.980	748.51	729.67	14.938	826.11	804.93	16.159	903.71	880.02	17.325
673.40	656.77	14.065	751.01	732.09	15.038	828.61	807.35	16.224	906.22	882.45	17.333
675.91	659.21	14.091	753.51	734.52	15.077	831.12	809.78	16.246	908.72	884.87	17.377
678.41	661.63	14.117	756.02	736.96	15.112	833.62	812.20	16.307	911.22	887.28	17.419
680.91	664.06	14.135	758.52	739.38	15.148	836.12	814.62	16.333	913.73	889.71	17.444
683.42	666.50	14.150	761.02	741.81	15.179	838.63	817.05	16.361	916.23	892.13	17.478
685.92	668.93	14.189	763.53	744.24	15.215	841.13	819.47	16.393	918.73	894.54	17.513
688.42	671.35	14.226	766.03	746.67	15.249	843.63	821.89	16.407	921.24	896.97	17.551
690.93	673.79	14.240	768.53	749.09	15.284	846.14	824.32	16.436	923.74	899.38	17.600
693.43	676.22	14.296	771.04	751.53	15.319	848.64	826.74	16.458	926.24	901.80	17.641
695.93	678.64	14.317	773.54	753.95	15.352	851.14	829.16	16.482	928.75	904.23	17.663
698.44	681.08	14.352	776.04	756.38	15.386	853.65	831.59	16.577	931.25	906.64	17.704

Appendix 1. Temperature data in OL-KR56 (cont.)

Logging depth [m]	Vertical depth [m]	Temperature [°C]	Logging depth [m]	Vertical depth [m]	Temperature [°C]	Logging depth [m]	Vertical depth [m]	Temperature [°C]	Logging depth [m]	Vertical depth [m]	Temperature [°C]
933.75	909.06	17.729	1011.36	983.98	18.879	1088.96	1058.73	20.050	1166.57	1133.24	21.295
936.26	911.48	17.782	1013.86	986.39	18.905	1091.47	1061.14	20.071	1169.07	1135.64	21.324
938.76	913.90	17.808	1016.36	988.80	18.948	1093.97	1063.55	20.089	1171.57	1138.03	21.327
941.26	916.31	17.826	1018.87	991.22	18.980	1096.47	1065.95	20.101	1174.08	1140.44	21.353
943.77	918.73	17.846	1021.37	993.63	19.033	1098.98	1068.36	20.152	1176.58	1142.83	21.368
946.27	921.15	17.915	1023.87	996.04	19.055	1101.48	1070.77	20.220	1179.08	1145.23	21.371
948.77	923.56	18.012	1026.38	998.46	19.109	1103.98	1073.17	20.261	1181.59	1147.63	21.526
951.28	925.99	18.042	1028.88	1000.87	19.109	1106.49	1075.58	20.301	1184.09	1150.02	21.547
953.78	928.40	18.049	1031.38	1003.28	19.181	1108.99	1077.98	20.340	1186.59	1152.42	21.564
956.28	930.82	18.079	1033.89	1005.70	19.218	1111.49	1080.39	20.383	1189.10	1154.82	21.577
958.79	933.24	18.128	1036.39	1008.11	19.258	1114.00	1082.80	20.424	1191.60	1157.22	21.721
961.29	935.66	18.137	1038.89	1010.52	19.302	1116.50	1085.20	20.466			
963.79	938.07	18.172	1041.40	1012.94	19.329	1119.00	1087.60	20.503			
966.30	940.49	18.219	1043.90	1015.35	19.379	1121.51	1090.01	20.583			
968.80	942.91	18.241	1046.41	1017.77	19.378	1124.01	1092.41	20.603			
971.30	945.32	18.279	1048.91	1020.18	19.454	1126.51	1094.81	20.615			
973.81	947.75	18.304	1051.41	1022.58	19.466	1129.02	1097.22	20.627			
976.31	950.16	18.323	1053.92	1025.00	19.522	1131.52	1099.62	20.697			
978.81	952.57	18.338	1056.42	1027.41	19.538	1134.02	1102.02	20.737			
981.32	955.00	18.469	1058.92	1029.81	19.601	1136.53	1104.43	20.777			
983.82	957.41	18.502	1061.43	1032.23	19.641	1139.03	1106.83	20.816			
986.32	959.82	18.517	1063.93	1034.64	19.654	1141.53	1109.23	20.858			
988.83	962.24	18.543	1066.43	1037.04	19.700	1144.04	1111.64	20.977			
991.33	964.66	18.569	1068.94	1039.46	19.729	1146.54	1114.03	20.979			
993.83	967.07	18.620	1071.44	1041.87	19.779	1149.04	1116.43	21.006			
996.34	969.49	18.667	1073.94	1044.27	19.810	1151.55	1118.84	21.028			
998.84	971.90	18.713	1076.45	1046.69	19.836	1154.05	1121.24	21.048			
1001.34	974.31	18.709	1078.95	1049.09	19.876	1156.55	1123.63	21.058			
1003.85	976.74	18.745	1081.45	1051.50	19.904	1159.06	1126.04	21.060			
1006.35	979.15	18.785	1083.96	1053.91	19.965	1161.56	1128.44	21.239			
1008.85	981.56	18.833	1086.46	1056.32	19.993	1164.06	1130.83	21.276			

Appendix 2: Results of laboratory measurements at room temperature

Appendix 2. Measured rock thermal rock properties (at room temperature), rock types and foliation angles of OL-KR56 core samples.

Sample code	Logging depth [m]	Vertical depth[m]	Rock type	Angle of foliation [°]	Conductivity [W m ⁻¹ K ⁻¹]	Specific heat [J kg ⁻¹ K ⁻¹]	Density [kg m ⁻³]	Diffusivity [10 ⁻⁶ m ² s ⁻¹]
OL-KR57B-2.70	2.70	2.69	VGN	9	1.89	737	2799	0.91
OL-KR57B-5.03	5.03	5.00	VGN	28	2.47	733	2733	1.23
OL-KR57B-10.02	10.02	9.96	VGN	38	2.31	738	2734	1.15
OL-KR57B-14.99	14.99	14.89	VGN	27	2.34	725	2769	1.17
OL-KR57B-20.00	20.00	19.84	DGN	24	3.24	749	2767	1.56
OL-KR57B-24.93	24.93	24.71	PGR	49	2.65	717	2646	1.40
OL-KR57B-29.97	29.97	29.68	TGG	31	2.14	711	2705	1.11
OL-KR57B-34.94	34.94	34.56	TGG	38	2.15	715	2722	1.10
OL-KR56-39.94	39.94	39.47	PGR		3.11	725	2601	1.65
OL-KR57B-39.99	39.99	39.52	TGG	36	2.20	731	2707	1.11
OL-KR56-44.02	44.02	43.47	PGR		1.49	725	2596	0.79
OL-KR56-50.09	50.09	49.43	PGR		2.21	740	2583	1.15
OL-KR56-54.84	54.84	54.09	PGR		2.21	804	2596	1.06
OL-KR56-59.06	59.06	58.22	PGR		2.29	735	2630	1.18
OL-KR56-64.99	64.99	64.04	VGN	14	2.58	764	2719	1.24
OL-KR56-69.94	69.94	68.89	MGN	60	2.13	761	2780	1.01
OL-KR56-74.88	74.88	73.73	VGN	69	2.67	693	2648	1.46
OL-KR56-79.85	79.85	78.60	MGN		2.13	734	2834	1.03
OL-KR56-85.11	85.11	83.74	MGN	65	2.04	743	2911	0.94
OL-KR56-89.74	89.74	88.27	MGN	61	2.03	738	2788	0.99
OL-KR56-94.60	94.60	93.02	VGN	55	2.33	747	2754	1.13
OL-KR56-100.00	100.00	98.30	MGN	48	1.94	819	2780	0.85
OL-KR56-105.02	105.02	103.20	MGN	41	2.36	741	2857	1.11
OL-KR56-109.55	109.55	107.63	PGR	41	2.22	721	2687	1.15
OL-KR56-114.86	114.86	112.82	PGR		3.00	720	2692	1.55
OL-KR56-120.00	120.00	117.84	MGN	66	2.30	724	2785	1.14
OL-KR56-124.97	124.97	122.69	DGN	38	2.75	736	2677	1.40
OL-KR56-129.99	129.99	127.59	MGN	66	2.63	735	2729	1.31
OL-KR56-135.00	135.00	132.48	MGN	62	2.05	752	2975	0.92
OL-KR56-140.00	140.00	137.37	PGR		2.57	722	2602	1.37
OL-KR56-145.11	145.11	142.36	MGN	27	2.51	736	2750	1.24

Rock types: VGN, veined gneiss; TGG, tonalitic-granodioritic-granitic gneiss; DGN, diatexitic gneiss; MGN, mica gneiss; PGR, pegmatitic granite

Appendix 2. Measured rock thermal rock properties (at room temperature), rock types and foliation angles of OL-KR56 core samples (cont.)

Sample code	Logging depth [m]	Vertical depth[m]	Rock type	Angle of foliation [°]	Conductivity [W m ⁻¹ K ⁻¹]	Specific heat [J kg ⁻¹ K ⁻¹]	Density [kg m ⁻³]	Diffusivity [10 ⁻⁶ m ² s ⁻¹]
OL-KR56-149.91	149.91	147.05	DGN	40	2.75	726	2638	1.44
OL-KR56-154.90	154.90	151.93	DGN	45	2.85	730	2706	1.44
OL-KR56-160.00	160.00	156.91	DGN	35	2.93	745	2685	1.47
OL-KR56-165.07	165.07	161.86	VGN	5	2.90	730	2762	1.44
OL-KR56-170.00	170.00	166.68	PGR	60	3.65	747	2709	1.80
OL-KR56-175.03	175.03	171.59	DGN	35	2.77	720	2668	1.44
OL-KR56-179.94	179.94	176.39	DGN	59	2.52	768	2708	1.21
OL-KR56-184.90	184.90	181.24	MGN	69	2.01	760	2898	0.91
OL-KR56-190.02	190.02	186.24	DGN	58	1.83	724	2787	0.91
OL-KR56-195.00	195.00	191.10	DGN	42	2.87	747	2692	1.43
OL-KR56-200.06	200.06	196.04	VGN	44	2.77	751	2763	1.33
OL-KR56-205.03	205.03	200.90	VGN	23	2.87	765	2770	1.35
OL-KR56-209.84	209.84	205.59	VGN	24	2.95	777	2760	1.38
OL-KR56-214.97	214.97	210.60	VGN	44	2.83	749	2748	1.37
OL-KR56-219.32	219.32	214.85	VGN	23	2.87	855	2738	1.22
OL-KR56-225.00	225.00	220.39	DGN	22	2.93	768	2744	1.39
OL-KR56-229.98	229.98	225.25	DGN	24	2.87	734	2704	1.44
OL-KR56-234.95	234.95	230.10	VGN	33	3.23	741	2744	1.59
OL-KR56-240.10	240.10	235.13	VGN	31	2.69	744	2684	1.35
OL-KR56-244.96	244.96	239.87	VGN	10	2.70	745	2727	1.33
OL-KR56-249.96	249.96	244.74	VGN	27	2.49	759	2722	1.21
OL-KR56-255.05	255.05	249.71	DGN	42	2.48	748	2763	1.20
OL-KR56-260.00	260.00	254.54	DGN	20	3.29	741	2700	1.64
OL-KR56-265.10	265.10	259.51	DGN	27	2.81	753	2772	1.35
OL-KR56-270.04	270.04	264.32	PRG	36	3.09	735	2631	1.60
OL-KR56-274.88B	274.88	269.04	PGR	31	2.62	744	2705	1.30
OL-KR56-274.88	274.88	269.04	PGR	36	2.85	739	2690	1.43
OL-KR56-280.02	280.02	274.05	VGN	37	2.47	722	2722	1.26
OL-KR56-285.05	285.05	278.96	PGR		2.74	721	2631	1.44
OL-KR56-289.94B	289.94	283.72	VGN	60	1.74	758	2752	0.83
OL-KR56-289.94	289.94	283.72	VGN	54	2.02	740	2735	1.00

Rock types: VGN, veined gneiss; TGG, tonalitic-granodioritic-granitic gneiss; DGN, diatexitic gneiss; MGN, mica gneiss; PGR, pegmatitic granite

Appendix 2. Measured rock thermal rock properties (at room temperature), rock types and foliation angles of OL-KR56 core samples (cont.)

Sample code	Logging depth [m]	Vertical depth[m]	Rock type	Angle of foliation [°]	Conductivity [W m ⁻¹ K ⁻¹]	Specific heat [J kg ⁻¹ K ⁻¹]	Density [kg m ⁻³]	Diffusivity [10 ⁻⁶ m ² s ⁻¹]
OL-KR56-295.12B	295.12	288.77	DGN	15	2.86	748	2711	1.41
OL-KR56-295.12	295.12	288.77	DGN	29	2.89	739	2693	1.45
OL-KR56-299.99	299.99	293.52	DGN	49	1.80	765	2721	0.87
OL-KR56-304.66	304.66	298.07	TGG		2.98	733	2636	1.54
OL-KR56-310.24	310.24	303.51	TGG	26	2.18	724	2811	1.07
OL-KR56-314.98	314.98	308.13	TGG	66	1.70	730	2812	0.83
OL-KR56-319.94	319.94	312.96	DGN	58	1.98	742	2754	0.97
OL-KR56-324.95	324.95	317.84	MGN		2.22	713	2722	1.15
OL-KR56-330.02	330.02	322.78	PGR		3.23	706	2616	1.75
OL-KR56-334.92	334.92	327.55	VGN	28	2.07	750	2766	1.00
OL-KR56-339.91UP	339.91	332.41	PGR		3.20	742	2629	1.64
OL-KR56-339.91D	339.91	332.41	PGR	69	3.35	757	2686	1.65
OL-KR56-345.18	345.18	337.54	PGR	50	2.73	761	2653	1.35
OL-KR56-350.09	350.09	342.32	PGR		2.62	749	2600	1.34
OL-KR56-354.90	354.90	347.01	DGN	49	2.62	742	2665	1.33
OL-KR56-359.96	359.96	351.93	MGN		3.67	756	2984	1.63
OL-KR56-364.29	364.29	356.15	PGR		3.03	763	2690	1.48
OL-KR56-370.01	370.01	361.72	TGG	25	2.78	776	2756	1.30
OL-KR56-375.06	375.06	366.63	DGN	47	3.45	763	2703	1.67
OL-KR56-379.93	379.93	371.37	DGN	19	2.71	760	2756	1.29
OL-KR56-385.02B	385.02	376.33	PGR		2.76	711	2602	1.49
OL-KR56-385.02	385.02	376.33	PGR		2.70	727	2595	1.43
OL-KR56-390.15	390.15	381.32	DGN	50	2.92	745	2712	1.45
OL-KR56-395.04	395.04	386.08	VGN	48	2.90	766	2703	1.40
OL-KR56-399.96B	399.96	390.87	PGR		2.29	763	2616	1.15
OL-KR56-399.96	399.96	390.87	PGR		2.77	730	2613	1.45
OL-KR56-404.85	404.85	395.63	DGN	44	2.83	782	2693	1.34
OL-KR56-409.87	409.87	400.52	DGN	48	2.79	752	2685	1.38
OL-KR56-414.97	414.97	405.48	VGN	48	2.51	766	2763	1.19
OL-KR56-419.92B	419.92	410.30	VGN	26	2.58	769	2742	1.22
OL-KR56-419.92	419.92	410.30	VGN	41	2.54	768	2728	1.21

Rock types: VGN, veined gneiss; TGG, tonalitic-granodioritic-granitic gneiss; DGN, diatexitic gneiss; MGN, mica gneiss; PGR, pegmatitic granite

Appendix 2. Measured rock thermal rock properties (at room temperature), rock types and foliation angles of OL-KR56 core samples (cont.)

Sample code	Logging depth [m]	Vertical depth[m]	Rock type	Angle of foliation [°]	Conductivity [W m ⁻¹ K ⁻¹]	Specific heat [J kg ⁻¹ K ⁻¹]	Density [kg m ⁻³]	Diffusivity [10 ⁻⁶ m ² s ⁻¹]
OL-KR56-424.87	424.87	415.11	DGN	60	2.73	757	2740	1.32
OL-KR56-430.00	430.00	420.11	PGR		2.02	748	2638	1.02
OL-KR56-435.01	435.01	424.98	PGR		2.19	737	2631	1.13
OL-KR56-440.07	440.07	429.91	DGN	71	2.67	773	2736	1.26
OL-KR56-445.01	445.01	434.71	DGN	70	2.84	740	2655	1.45
OL-KR56-449.98	449.98	439.55	DGN	43	2.60	774	2740	1.23
OL-KR56-455.01	455.01	444.44	DGN	73	1.40	785	2937	0.61
OL-KR56-459.89	459.89	449.19	PGR		2.59	724	2635	1.36
OL-KR56-464.97	464.97	454.14	PGR	46	2.72	741	2691	1.37
OL-KR56-470.02	470.02	459.05	PGR		2.48	724	2597	1.32
OL-KR56-475.02	475.02	463.92	DGN	67	2.80	748	2659	1.41
OL-KR56-479.97	479.97	468.73	PGR		2.43	750	2587	1.25
OL-KR56-484.93	484.93	473.56	PGR		2.17	755	2580	1.12
OL-KR56-490.06	490.06	478.55	DGN	18	2.44	748	2717	1.20
OL-KR56-494.97	494.97	483.33	PGR		2.66	738	2642	1.36
OL-KR56-500.32	500.32	488.53	VGN	35	1.45	739	2738	0.72
OL-KR56-504.87	504.87	492.96	VGN	31	2.62	749	2783	1.26
OL-KR56-510.15	510.15	498.09	DGN	43	2.39	760	2688	1.17
OL-KR56-514.90	514.90	502.71	DGN	32	2.60	781	2749	1.21
OL-KR56-520.15	520.15	507.82	DGN	27	3.10	783	2775	1.43
OL-KR56-524.93	524.93	512.47	DGN	38	2.71	737	2683	1.37
OL-KR56-530.01	530.01	517.41	VGN	36	2.71	729	2753	1.35
OL-KR56-534.98	534.98	522.25	PGR		3.26	721	2633	1.72
OL-KR56-539.85	539.85	526.98	VGN	59	3.25	736	2725	1.62
OL-KR56-544.95	544.95	531.94	PGR		3.35	740	2648	1.71
OL-KR56-549.91B	549.91	536.77	VGN	31	3.14	751	2723	1.54
OL-KR56-549.91	549.91	536.77	VGN	37	3.19	742	2706	1.59
OL-KR56-555.00	555.00	541.72	PGR		2.98	737	2633	1.54
OL-KR56-560.16	560.16	546.74	PGR		3.27	737	2614	1.70
OL-KR56-565.00	565.00	551.44	PGR		2.82	723	2591	1.50
OL-KR56-569.83B	569.83	556.14	DGN	51	2.66	718	2726	1.36

Rock types: VGN, veined gneiss; TGG, tonalitic-granodioritic-granitic gneiss; DGN, diatexitic gneiss; MGN, mica gneiss; PGR, pegmatitic granite

Appendix 2. Measured rock thermal rock properties (at room temperature), rock types and foliation angles of OL-KR56 core samples (cont.)

Sample code	Logging depth [m]	Vertical depth[m]	Rock type	Angle of foliation [°]	Conductivity [W m ⁻¹ K ⁻¹]	Specific heat [J kg ⁻¹ K ⁻¹]	Density [kg m ⁻³]	Diffusivity [10 ⁻⁶ m ² s ⁻¹]
OL-KR56-569.83	569.83	556.14	DGN	45	2.17	753	2688	1.07
OL-KR56-574.91	569.83	556.14	PGR		2.99	730	2603	1.57
OL-KR56-580.08	580.08	566.11	PGR		3.76	701	2653	2.02
OL-KR56-584.99	584.99	570.88	PGR	54	3.17	715	2657	1.67
OL-KR56-589.89B	589.89	575.64	DGN	57	2.77	732	2638	1.43
OL-KR56-589.89	589.89	575.64	DGN	59	2.71	720	2692	1.40
OL-KR56-594.95	594.95	580.56	PGR		2.66	717	2643	1.40
OL-KR56-600.03	600.03	585.50	PGR		2.93	729	2629	1.53
OL-KR56-605.00	605.00	590.33	DGN	61	3.05	724	2714	1.55
OL-KR56-609.99	609.99	595.19	VGN	16	3.59	722	2710	1.84
OL-KR56-615.00	615.00	600.05	PGR	14	2.77	728	2660	1.43
OL-KR56-620.08	620.08	604.99	DGN	65	2.77	756	2763	1.32
OL-KR56-625.01	625.01	609.78	DGN	46	2.80	730	2744	1.40
OL-KR56-630.06B	630.06	614.69	MGN	58	2.30	734	2777	1.13
OL-KR56-630.06	630.06	614.69	MGN	68	1.79	730	2788	0.88
OL-KR56-634.99	634.99	619.48	DGN	30	5.97	735	2777	2.93
OL-KR56-640.00	640.00	624.35	VGN	42	2.80	716	2749	1.42
OL-KR56-645.01	645.01	629.21	VGN	42	2.92	731	2733	1.46
OL-KR56-649.92	649.92	633.98	PGR		2.67	731	2649	1.38
OL-KR56-654.99	654.99	638.91	PGR	37	2.60	736	2710	1.30
OL-KR56-660.00	660.00	643.77	PGR		3.08	728	2643	1.60
OL-KR56-664.90	664.90	648.53	DGN	51	2.82	721	2698	1.45
OL-KR56-670.45	670.45	653.92	VGN	48	2.78	747	2810	1.33
OL-KR56-675.00	675.00	658.33	DGN	47	2.95	754	2712	1.45
OL-KR56-679.93	679.93	663.12	PGR		2.62	735	2584	1.38
OL-KR56-684.93	684.93	667.97	DGN	22	2.79	750	2669	1.39
OL-KR56-689.94	689.94	672.84	DGN	66	2.21	748	2788	1.06
OL-KR56-694.98	694.98	677.73	PGR		3.14	716	2654	1.65
OL-KR56-700.73	700.73	683.31	DGN	42	3.15	733	2643	1.63
OL-KR56-705.00	705.00	687.45	VGN	23	2.75	773	2758	1.29
OL-KR56-710.01	710.01	692.32	DGN	43	3.31	738	2686	1.67

Rock types: VGN, veined gneiss; TGG, tonalitic-granodioritic-granitic gneiss; DGN, diatexitic gneiss; MGN, mica gneiss; PGR, pegmatitic granite

Appendix 2. Measured rock thermal rock properties (at room temperature), rock types and foliation angles of OL-KR56 core samples (cont.)

Sample code	Logging depth [m]	Vertical depth[m]	Rock type	Angle of foliation [°]	Conductivity [W m ⁻¹ K ⁻¹]	Specific heat [J kg ⁻¹ K ⁻¹]	Density [kg m ⁻³]	Diffusivity [10 ⁻⁶ m ² s ⁻¹]
OL-KR56-714.99	714.99	697.15	PGR		2.19	720	2615	1.16
OL-KR56-720.01	720.01	702.02	DGN	33	2.67	747	2746	1.30
OL-KR56-724.85	724.85	706.72	MGN	28	2.59	746	2726	1.27
OL-KR56-729.98	729.98	711.70	VGN	77	0.96	761	2764	0.46
OL-KR56-734.97	734.97	716.54	PGR	21	2.24	757	2640	1.12
OL-KR56-740.02	740.02	721.44	DGN	18	2.44	768	2792	1.14
OL-KR56-745.07	745.07	726.34	PGR		2.46	762	2647	1.22
OL-KR56-750.03	750.03	731.15	PGR		3.09	759	2616	1.56
OL-KR56-754.89B	754.89	735.87	VGN	58	1.88	773	2730	0.89
OL-KR56-754.89	754.89	735.87	VGN	75	2.03	767	2738	0.97
OL-KR56-759.89	759.89	740.72	DGN	50	2.45	770	2739	1.16
OL-KR56-765.06	765.06	745.74	VGN	21	2.80	748	2723	1.37
OL-KR56-770.02	770.02	750.55	PGR		2.87	756	2605	1.45
OL-KR56-780.10	780.10	760.33	MGN	20	3.11	768	2708	1.49
OL-KR56-784.94B	784.94	765.02	MGN	66	2.25	712	2830	1.12
OL-KR56-784.94	784.94	765.02	MGN		2.26	727	2825	1.10
OL-KR56-789.96	789.96	769.89	PGR		3.09	749	2601	1.58
OL-KR56-794.98	794.98	774.76	TGG	19	2.23	745	2776	1.08
OL-KR56-799.97	799.97	779.60	TGG	43	2.21	744	2797	1.06
OL-KR56-805.01	805.01	784.49	MGN	44	2.26	748	2762	1.09
OL-KR56-809.97	809.97	789.29	TGG	44	2.12	747	2749	1.03
OL-KR56-814.99	814.99	794.16	TGG	35	2.50	736	2752	1.23
OL-KR56-819.98	819.98	799.00	VGN	53	1.83	741	2772	0.89
OL-KR56-824.99	824.99	803.85	VGN	28	2.53	732	2738	1.26
OL-KR56-829.96	829.96	808.67	DGN	28	1.83	750	2740	0.89
OL-KR56-834.92	834.92	813.47	PGR		2.73	727	2596	1.45
OL-KR56-840.00	840.00	818.39	DGN	23	1.47	762	2782	0.69
OL-KR56-844.92	844.92	823.15	MGN	8	2.21	744	2772	1.07
OL-KR56-850.00	850.00	828.07	DGN	21	2.29	753	2723	1.12
OL-KR56-855.00	855.00	832.91	DGN	32	2.40	717	2758	1.21
OL-KR56-860.00B	860.00	837.75	VGN	44	2.16	741	2745	1.06

Rock types: VGN, veined gneiss; TGG, tonalitic-granodioritic-granitic gneiss; DGN, diatexitic gneiss; MGN, mica gneiss; PGR, pegmatitic granite

Appendix 2. Measured rock thermal rock properties (at room temperature), rock types and foliation angles of OL-KR56 core samples (cont.)

Sample code	Logging depth [m]	Vertical depth[m]	Rock type	Angle of foliation [°]	Conductivity [W m ⁻¹ K ⁻¹]	Specific heat [J kg ⁻¹ K ⁻¹]	Density [kg m ⁻³]	Diffusivity [10 ⁻⁶ m ² s ⁻¹]
OL-KR56-860.00	860.00	837.75	VGN	53	2.27	749	2730	1.11
OL-KR56-864.99B	864.99	842.58	MGN	48	1.69	714	2772	0.85
OL-KR56-864.99	864.99	842.58	MGN	53	2.26	757	2765	1.08
OL-KR56-869.98	869.98	847.41	VGN	59	1.92	743	2756	0.94
OL-KR56-875.00	875.00	852.26	VGN	24	2.18	741	2765	1.06
OL-KR56-879.97	879.97	857.07	DGN	24	2.10	741	2671	1.06
OL-KR56-884.96	884.96	861.90	DGN	53	2.11	725	2781	1.04
OL-KR56-889.96	889.96	866.74	VGN	32	2.29	749	2738	1.12
OL-KR56-895.01	895.01	871.62	DGN	61	2.81	731	2651	1.45
OL-KR56-899.99	899.99	876.43	VGN	54	2.24	735	2755	1.11
OL-KR56-905.00	899.99	876.43	PGR		2.69	729	2632	1.40
OL-KR56-909.97	909.97	886.08	PGR		2.73	761	2608	1.37
OL-KR56-915.03Y	915.03	890.98	VGN	52	1.92	750	2746	0.93
OL-KR56-915.03	915.03	890.98	VGN	58	1.83	766	2739	0.87
OL-KR56-919.96	919.96	895.74	VGN	26	2.68	730	2747	1.34
OL-KR56-924.99B	924.99	900.60	PGR		2.71	724	2613	1.43
OL-KR56-924.99	924.99	900.60	PGR		2.71	732	2676	1.38
OL-KR56-929.98	929.98	905.42	PGR		2.70	736	2609	1.40
OL-KR56-934.90	934.90	910.18	VGN	18	2.56	740	2729	1.27
OL-KR56-939.98	939.98	915.08	VGN	30	2.48	725	2695	1.27
OL-KR56-944.98B	944.98	919.91	PGR	43	2.10	717	2632	1.11
OL-KR56-944.98	944.98	919.91	PGR	76	2.30	727	2628	1.20
OL-KR56-949.89	949.89	924.66	DGN	10	2.54	760	2699	1.24
OL-KR56-954.84	954.84	929.44	DGN	33	1.82	740	2800	0.88
OL-KR56-960.01	960.01	934.43	PGR		3.24	727	2633	1.69
OL-KR56-964.99	964.99	939.24	VGN	49	2.62	728	2723	1.32
OL-KR56-969.93	969.93	944.01	PGR		3.22	728	2899	1.52
OL-KR56-974.92	974.92	948.83	VGN	2	2.81	738	2681	1.42
OL-KR56-979.98	979.98	953.71	VGN	46	1.96	754	2807	0.92
OL-KR56-984.95	984.95	958.51	DGN	31	2.91	752	2722	1.42
OL-KR56-989.96	989.96	963.35	PGR		1.59	787	2522	0.80

Rock types: VGN, veined gneiss; TGG, tonalitic-granodioritic-granitic gneiss; DGN, diatexitic gneiss; MGN, mica gneiss; PGR, pegmatitic granite

Appendix 2. Measured rock thermal rock properties (at room temperature), rock types and foliation angles of OL-KR56 core samples (cont.)

Sample code	Logging depth [m]	Vertical depth[m]	Rock type	Angle of foliation [°]	Conductivity [W m ⁻¹ K ⁻¹]	Specific heat [J kg ⁻¹ K ⁻¹]	Density [kg m ⁻³]	Diffusivity [10 ⁻⁶ m ² s ⁻¹]
OL-KR56-994.98	994.98	968.19	DGN	33	3.62	740	2700	1.81
OL-KR56-1000.07	1000.07	973.10	MGN	33	2.58	772	2729	1.22
OL-KR56-1005.01	1005.01	977.87	MGN	63	2.96	734	2746	1.47
OL-KR56-1009.99	1009.99	982.67	VGN	52	2.26	746	2721	1.11
OL-KR56-1014.98	1014.98	987.48	MGN	51	2.25	739	2706	1.13
OL-KR56-1019.98	1019.98	992.30	MGN	73	2.18	739	2736	1.08
OL-KR56-1025.00	1025.00	997.14	MGN	15	2.62	719	2702	1.35
OL-KR56-1030.06	1030.06	1002.02	VGN	11	2.61	746	2704	1.29
OL-KR56-1034.95	1034.95	1006.74	VGN	66	2.54	747	2703	1.26
OL-KR56-1039.98	1039.98	1011.58	VGN	55	2.44	745	2687	1.22
OL-KR56-1044.90	1044.90	1016.32	VGN	25	2.32	762	2740	1.11
OL-KR56-1049.99B	1049.99	1021.23	DGN	51	1.97	766	2772	0.93
OL-KR56-1049.99	1049.99	1021.23	DGN	48	2.08	752	2777	0.99
OL-KR56-1054.86	1054.86	1025.92	VGN	22	2.80	741	2675	1.41
OL-KR56-1060.16	1060.16	1031.02	VGN	13	2.29	736	2728	1.14
OL-KR56-1065.02	1065.02	1035.70	PGR		2.26	732	2592	1.19
OL-KR56-1069.89	1069.89	1040.38	DGN	39	2.44	749	2779	1.17
OL-KR56-1074.98	1074.98	1045.28	VGN	47	2.61	755	2771	1.25
OL-KR56-1079.96	1079.96	1050.08	VGN	28	2.13	741	2757	1.04
OL-KR56-1084.98	1084.98	1054.91	VGN	25	2.95	743	2709	1.47
OL-KR56-1090.01	1090.01	1059.75	VGN	0	2.79	753	2705	1.37
OL-KR56-1095.00	1095.00	1064.54	VGN	29	2.38	750	2798	1.13
OL-KR56-1099.89	1099.89	1069.25	VGN	64	2.85	725	2722	1.44
OL-KR56-1105.00	1105.00	1074.16	VGN	28	2.50	747	2748	1.22
OL-KR56-1109.97	1109.97	1078.93	VGN	18	2.07	748	2748	1.01
OL-KR56-1115.03	1115.03	1083.79	VGN	30	2.42	730	2710	1.22
OL-KR56-1119.98	1119.98	1088.55	VGN	21	2.54	751	2755	1.23
OL-KR56-1125.05	1125.05	1093.42	VGN	47	2.60	745	2780	1.26
OL-KR56-1129.98	1129.98	1098.15	DGN	29	2.59	736	2655	1.33
OL-KR56-1135.00	1135.00	1102.97	VGN	34	2.69	748	2812	1.28
OL-KR56-1140.01	1140.01	1107.77	MGN	61	2.58	752	2738	1.25

Rock types: VGN, veined gneiss; TGG, tonalitic-granodioritic-granitic gneiss; DGN, diatexitic gneiss; MGN, mica gneiss; PGR, pegmatitic granite

Appendix 2. *Measured rock thermal rock properties (at room temperature), rock types and foliation angles of OL-KR56 core samples (cont.)*

Sample code	Logging depth [m]	Vertical depth[m]	Rock type	Angle of foliation [°]	Conductivity [W m ⁻¹ K ⁻¹]	Specific heat [J kg ⁻¹ K ⁻¹]	Density [kg m ⁻³]	Diffusivity [10 ⁻⁶ m ² s ⁻¹]
OL-KR56-1144.95	1144.95	1112.51	DGN	11	2.48	747	2781	1.19
OL-KR56-1149.94	1149.94	1117.30	VGN	13	2.38	737	2780	1.16
OL-KR56-1155.02B	1155.02	1122.17	PGR	41	2.90	722	2661	1.51
OL-KR56-1155.02	1155.02	1122.17	PGR	48	2.97	733	2656	1.53
OL-KR56-1160.00	1160.00	1126.94	VGN	29	2.81	740	2709	1.40
OL-KR56-1165.00	1165.00	1131.74	VGN	24	2.69	743	2721	1.33
OL-KR56-1170.01	1170.01	1136.54	VGN	28	2.88	728	2691	1.47
OL-KR56-1175.91	1175.91	1142.19	VGN	61	2.40	737	2715	1.20
OL-KR56-1180.00	1180.00	1146.11	VGN	29	2.44	726	2704	1.24
OL-KR56-1185.01	1185.01	1150.91	DGN	76	2.52	750	2719	1.24
OL-KR56-1189.92	1189.92	1155.61	VGN	14	2.58	728	2711	1.31
OL-KR56-1194.95B	1194.95	1160.43	VGN	41	2.08	753	2755	1.00
OL-KR56-1194.95	1194.95	1160.43	VGN	50	2.16	733	2740	1.08
OL-KR56-1199.97	1199.97	1165.23	PGR		2.89	726	2624	1.52

Rock types: VGN, veined gneiss; TGG, tonalitic-granodioritic-granitic gneiss; DGN, diatexitic gneiss; MGN, mica gneiss; PGR, pegmatitic granite